

ARTICLE



<https://doi.org/10.1038/s41467-022-31161-2>

OPEN

# Trapping and detecting nanoplastics by MXene-derived oxide microrobots

Mario Urso <sup>1</sup>, Martina Ussia <sup>1</sup>, Filip Novotný<sup>1,2</sup> & Martin Pumera <sup>1,2,3,4</sup>✉

Nanoplastic pollution, the final product of plastic waste fragmentation in the environment, represents an increasing concern for the scientific community due to the easier diffusion and higher hazard associated with their small sizes. Therefore, there is a pressing demand for effective strategies to quantify and remove nanoplastics in wastewater. This work presents the “on-the-fly” capture of nanoplastics in the three-dimensional (3D) space by multi-functional MXene-derived oxide microrobots and their further detection. A thermal annealing process is used to convert  $\text{Ti}_3\text{C}_2\text{T}_x$  MXene into photocatalytic multi-layered  $\text{TiO}_2$ , followed by the deposition of a Pt layer and the decoration with magnetic  $\gamma\text{-Fe}_2\text{O}_3$  nanoparticles. The MXene-derived  $\gamma\text{-Fe}_2\text{O}_3/\text{Pt}/\text{TiO}_2$  microrobots show negative photogravitaxis, resulting in a powerful fuel-free motion with six degrees of freedom under light irradiation. Owing to the unique combination of self-propulsion and programmable Zeta potential, the microrobots can quickly attract and trap nanoplastics on their surface, including the slits between multi-layer stacks, allowing their magnetic collection. Utilized as self-motile preconcentration platforms, they enable nanoplastics’ electrochemical detection using low-cost and portable electrodes. This proof-of-concept study paves the way toward the “on-site” screening of nanoplastics in water and its successive remediation.

<sup>1</sup>Future Energy and Innovation Laboratory, Central European Institute of Technology, Brno University of Technology, Purkyňova 123, 61200 Brno, Czech Republic. <sup>2</sup>Center for Advanced Functional Nanorobots, Department of Inorganic Chemistry, Faculty of Chemical Technology, University of Chemistry and Technology Prague, Technická 5, 166 28 Prague, Czech Republic. <sup>3</sup>Department of Chemical and Biomolecular Engineering, Yonsei University, 50 Yonsei-ro, Seodaemun-gu, Seoul 03722, Korea. <sup>4</sup>Department of Medical Research, China Medical University Hospital, China Medical University, No. 91 Hsueh-Shih Road, Taichung, Taiwan. ✉email: [martin.pumera@ceitec.vutbr.cz](mailto:martin.pumera@ceitec.vutbr.cz)

The images of marine environments full of plastic bags, bottles, and other plastic waste are impressed in our minds and mirror humankind's unpreparedness to manage them<sup>1,2</sup>. Unfortunately, the actual hazard of plastics is not restricted only to what is visible to our eyes. Plastic materials fragment into smaller pieces with sizes below 5 mm, called microplastics<sup>3</sup>. These can further break down into even smaller and more dangerous pieces (1–1000 nm), referred to as nanoplastics<sup>4–6</sup>. In fact, microplastics typically sediment on the seafloor, while nanoplastics remain suspended in water due to their lower weight<sup>7</sup>. Then, they are transported by the ocean currents, diffusing in short times. Because of their high surface-to-volume ratio, nanoplastics can absorb large amounts of toxic pollutants in water and serve as the substrate for the growth of pathogenic bacterial biofilms, increasing their toxicity<sup>7,8</sup>. Contrarily to the microplastics, they can easily penetrate tissues, posing serious risks to the health of all living beings<sup>9</sup>.

The detection of nanoplastics in water samples and their consequent removal is critical. Scanning electron microscopy (SEM) and transmission electron microscopy (TEM) allow for visualizing nanoplastics but do not provide other information about the plastic material<sup>10</sup>. Similarly, nanoparticle tracking analysis (NTA) measures the nanoplastics' size distribution and concentration by recording the scattered light from an incident light beam<sup>11</sup>. Mass spectrometry techniques are also promising for studying nanoplastics. In this regard, Mitrano and coworkers synthesized nanoplastics with a metallic core to monitor their fate in the environment through inductively coupled plasma mass spectrometry (ICP-MS)<sup>12</sup>. However, a strategy for the rapid and “on-site” screening of nanoplastics in water samples without the need for expensive laboratory instruments and specialized staff is missing<sup>13</sup>. Besides, the remediation of nanoplastics-contaminated waters is crucial. Conventional approaches for removing microplastics, such as filtration, are not suitable for nanoplastics due to their tiny size<sup>14</sup>. On the other hand, the concept of microplastics' capture by electrostatic forces using oppositely charged magnetic particles and their successive collection with magnets can be potentially extended to the nanoplastics<sup>15</sup>.

Micro/nanorobots, combining the unique physicochemical properties of micro/nanoscale materials with the autonomous motion ability and programmable functionalities, are revolutionizing all application fields, including environmental remediation<sup>16–18</sup>, sensing<sup>19,20</sup>, biomedicine<sup>21,22</sup>, and electronics<sup>23</sup>. Specifically, in water remediation, their active movement overcomes the limitation of passive diffusion and enhances the interaction with pollutants, accelerating the purification process<sup>24</sup>. Among the different micro/nanorobots, light-powered ones are particularly promising for this purpose since light is an abundant and powerful energy source to induce their motion and, at the same time, favor the photocatalytic degradation of pollutants through advanced oxidation processes<sup>25</sup>. The most investigated light-powered micro/nanorobot consists of a Janus particle formed by a photocatalytic semiconductor (TiO<sub>2</sub>, ZnO, Fe<sub>2</sub>O<sub>3</sub>) asymmetrically covered by a metal layer (Pt, Au)<sup>26–28</sup>. The metal layer deposition can be avoided for some intrinsically asymmetric microrobots (BiVO<sub>4</sub>, Bi<sub>2</sub>WO<sub>6</sub>), but they require small amounts of toxic H<sub>2</sub>O<sub>2</sub> fuel to move under light irradiation<sup>29,30</sup>. In the last years, light-powered micro/nanorobots have demonstrated remarkable potential for removing microplastics<sup>31</sup>. Au/Ni/TiO<sub>2</sub> micromotors have been used to remove microplastic debris in water<sup>32</sup>. Pt-Pd/Fe<sub>2</sub>O<sub>3</sub> microrobots were able to break the strong covalent bonds in polymer chains through the photo-Fenton reaction<sup>25</sup>. Fe<sub>3</sub>O<sub>4</sub>/BiVO<sub>4</sub> microrobots were used to degrade polylactic acid and polycaprolactone in a confined space<sup>33</sup>. Microplastics were enzymatically digested by magnetic field-powered mussel-inspired polydopamine@Fe<sub>3</sub>O<sub>4</sub>/lipase adhesive microrobots as an alternative to the photocatalytic degradation<sup>34</sup>. The adsorptive

bubble separation by bubble-propelled Fe<sub>2</sub>O<sub>3</sub>-MnO<sub>2</sub> micromotors has been also identified as an original mechanism for removing microplastics<sup>35</sup>. The main drawback of these microrobots is that the motion occurs at the bottom of the vessel, i.e., in 2D, due to the gravitational force. Since nanoplastics are suspended in water, a strong self-propulsion with six degrees of freedom is required to catch them properly in 3D.

MXenes are promising 2D materials for the fabrication of novel multifunctional microrobots<sup>36</sup>. They exhibit the general formula M<sub>n+1</sub>X<sub>n</sub>T<sub>x</sub> (*n* = 1, 2, 3), where M is an early transition metal (Ti, Mo, V), X is carbon and/or nitrogen, and T<sub>x</sub> is the surface-terminating functionality (–O, –F, –OH)<sup>37</sup>. MXenes are obtained from the selective etching of the A-element layers from a MAX phase, where A is a group IIIA or IVA element (Al, Si)<sup>37</sup>. This process results in “exfoliated” MXene microparticles with high surface area and an accordion-like multi-layered structure. Moreover, they exhibit high conductivity, excellent chemical stability, thermal conductivity, hydrophilicity, surface functionality, and environmental compatibility<sup>38</sup>. As a consequence, they have rapidly emerged in various applications, including water remediation<sup>39,40</sup>. Among the different MXenes, Ti<sub>3</sub>C<sub>2</sub>T<sub>x</sub> is the most studied one. Recently, Ti<sub>3</sub>C<sub>2</sub> nanoflakes, obtained after the delamination of the exfoliated MXene via ultrasonication, were turned into fuel-free UV-light-driven micromotors thanks to the deposition of a Pt layer on one side and the superficially formed TiO<sub>2</sub> in water<sup>41</sup>. These micromotors were able to boost the photocatalytic degradation of nitroaromatic explosives in water despite their low speed and small mean-squared displacement (MSD ~ 5 μm<sup>2</sup> in 3 s) compared to the other fuel-free light-driven micromotors<sup>25–28,42</sup>. In addition, the delamination involved the destruction of the peculiar multi-layered structure of the MXenes, which is promising for the nanoplastics' trapping.

This work demonstrates the “on-the-fly” capture of nanoplastics in water and their further electrochemical detection through self-propelled light-powered photocatalytic and magnetic MXene-derived oxide multi-layered microrobots. The concept is illustrated in Fig. 1. MXene-derived γ-Fe<sub>2</sub>O<sub>3</sub>/Pt/TiO<sub>2</sub> microrobots were fabricated through a thermal annealing process of exfoliated Ti<sub>3</sub>C<sub>2</sub>T<sub>x</sub> MXene microparticles, followed by the asymmetric deposition of a Pt layer and the subsequent decoration with magnetic γ-Fe<sub>2</sub>O<sub>3</sub> nanoparticles. The microrobots showed a negative photogravitactic behavior under UV-light irradiation, resulting in a powerful motion in 3D, and pH-programmable surface charge, which was adequately adjusted to maximize the electrostatic attraction of nanoplastics. SEM and NTA proved the rapid and effective nanoplastics trapping on the microrobots' surface, including the slits between the formerly MXene's multi-layer stacks. Acting as self-motile platforms for fast nanoplastics' preconcentration, the microrobots allowed to detect nanoplastics in water via electrochemical impedance spectroscopy (EIS), using low-cost and miniaturized screen-printed electrodes (SPEs).

## Results and discussion

**Fabrication and characterization of MXene-derived oxide multi-layered microrobots.** MXene-derived γ-Fe<sub>2</sub>O<sub>3</sub>/Pt/TiO<sub>2</sub> microrobots were prepared by thermal annealing of Ti<sub>3</sub>C<sub>2</sub>T<sub>x</sub> MXene, Pt layer deposition, and surface decoration with γ-Fe<sub>2</sub>O<sub>3</sub> nanoparticles. Figure 2a reports the scheme of the proposed fabrication procedure. Inspired by the work of Low et al., exfoliated Ti<sub>3</sub>C<sub>2</sub>T<sub>x</sub> MXene microparticles were converted into TiO<sub>2</sub> microparticles through a thermal annealing process in air at 550 °C, which has been previously identified as the optimal temperature to prepare TiO<sub>2</sub>/Ti<sub>3</sub>C<sub>2</sub> MXene composites<sup>43</sup>. The SEM image in Fig. 2b shows the surface morphology of the pristine Ti<sub>3</sub>C<sub>2</sub>T<sub>x</sub> MXene, which displays the characteristic

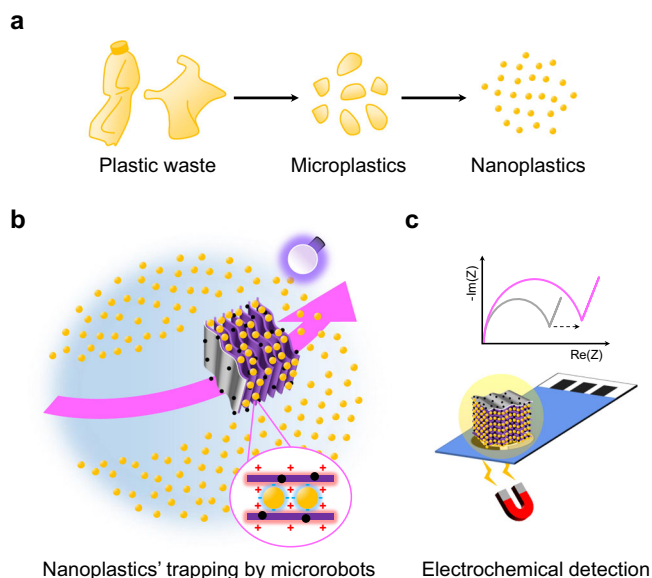


**Fig. 1** Light-powered magnetic MXene-derived  $\gamma\text{-Fe}_2\text{O}_3/\text{Pt}/\text{TiO}_2$  microrobots trap and detect nanoplastics. **a** Plastic waste in water fragments into micro- and nanoplastics. **b** Microrobots accelerate the removal of nanoplastics from water by trapping them on their surface, including the slits between multi-layer stacks, due to the combination of a powerful motion and a programmable electrostatic attraction. **c** Acting as self-propelled platforms for preconcentration, microrobots allow nanoplastics' detection by electrochemical impedance spectroscopy (EIS) using low-cost and portable electrodes in an electrolyte solution (yellow shading). The curves represent the impedance real ( $\text{Re}(Z)$ ) and imaginary ( $-\text{Im}(Z)$ ) parts as a function of the frequency (Nyquist plots) of microrobots before (gray) and after capturing nanoplastics (pink).

accordion-like structure consisting of several  $\text{Ti}_3\text{C}_2\text{T}_x$  multi-layer stacks with a smooth surface. A multi-layer stacks' thickness of  $\sim 20$  nm is measured from a high-resolution SEM image (Supplementary Fig. 1a). To preserve the MXene multi-layered structure for nanoplastics' trapping, the influence of thermal annealing duration on the morphology of the resulting  $\text{TiO}_2$  microparticles was investigated and optimized (Supplementary Fig. 2). After 120 min at  $550^\circ\text{C}$ , the MXene-derived  $\text{TiO}_2$  microparticles lose the multi-layered structure due to a significant expansion of the multi-layer stacks, resulting in a continuous and rough surface. By decreasing the duration to 60 min, 30 min, and 0 min,  $\text{TiO}_2$  multi-layer stacks' thickness and roughness decrease. Therefore, the optimal MXene-derived  $\text{TiO}_2$  microparticles were identified as those kept at  $550^\circ\text{C}$  for 0 min. For this reason, all results presented in the following relate to the 0 min annealing condition. Compared to the  $\text{Ti}_3\text{C}_2\text{T}_x$  MXene, these microparticles exhibit multi-layer stacks with a rougher surface and a larger thickness of  $\sim 50$  nm due to the in situ formed  $\text{TiO}_2$  nanoparticles (Supplementary Fig. 1b). MXene-derived  $\text{TiO}_2$  microparticles were asymmetrically covered with a 50 nm thick Pt layer by sputtering and mixed with  $\gamma\text{-Fe}_2\text{O}_3$  nanoparticles for 1 h at room temperature, fabricating light-powered magnetic microrobots. The SEM image in Fig. 2c indicates that the microrobots maintain the multi-layered structure after Pt deposition and  $\gamma\text{-Fe}_2\text{O}_3$  nanoparticles' loading. The latter can not be directly visualized on the microrobots due to the high surface roughness of the MXene-derived  $\text{TiO}_2$  microparticles and their small size ( $<50$  nm), as indicated by the SEM image of a cluster of  $\gamma\text{-Fe}_2\text{O}_3$  nanoparticles (Supplementary Fig. 3). The specific surface area of the  $\text{Ti}_3\text{C}_2\text{T}_x$  MXene and MXene-derived  $\gamma\text{-Fe}_2\text{O}_3/\text{Pt}/\text{TiO}_2$  microrobots was measured, finding  $3.9$  and  $6.8$   $\text{m}^2$   $\text{g}^{-1}$ , respectively. The former

agrees with previous works, reporting values between  $0.5$  and  $9$   $\text{m}^2$   $\text{g}^{-1}$  for multi-layer  $\text{Ti}_3\text{C}_2\text{T}_x$  MXene<sup>43,44</sup>. The larger surface area found for the microrobots is attributed to the thermal annealing process, converting the smooth  $\text{Ti}_3\text{C}_2\text{T}_x$  surface into  $\text{TiO}_2$  nanoparticles<sup>43</sup>, Pt layer deposition, and  $\gamma\text{-Fe}_2\text{O}_3$  nanoparticles' loading. The preservation of the multi-layered structure is crucial since it avoids sacrificing half of the microparticle's surface upon Pt deposition, as it occurs for smooth spherical particles. It should be noted that layered titanate presents a similar structure to the MXene-derived  $\text{TiO}_2$  microparticles, also having the advantage of simpler and cheaper preparation, in principle<sup>45</sup>. Nevertheless, the utilization of commercial exfoliated  $\text{Ti}_3\text{C}_2\text{T}_x$  MXene and its oxidation into  $\text{TiO}_2$  via thermal annealing was considered a more reproducible approach in this work.

X-ray diffraction (XRD) patterns in Fig. 2d prove the transformation of  $\text{Ti}_3\text{C}_2\text{T}_x$  into anatase  $\text{TiO}_2$ , which is considered the most photoactive among the different  $\text{TiO}_2$  crystal structures<sup>46</sup>. It is worth noting that Low and coworkers found small peaks attributed to  $\text{Ti}_3\text{C}_2$  in the XRD pattern of the annealed sample and demonstrated a  $\text{TiO}_2/\text{Ti}_3\text{C}_2$  core-shell structure by high-resolution TEM<sup>43</sup>. In this work, those XRD peaks were not found in the XRD pattern of any annealed sample, and thus the residual presence of the  $\text{Ti}_3\text{C}_2\text{T}_x$  MXene after the thermal annealing process was not claimed and further investigated. Hence, the optimal sample was referred to as an MXene-derived  $\text{TiO}_2$  rather than a  $\text{TiO}_2/\text{Ti}_3\text{C}_2$  MXene composite.

Light-absorption spectra of the  $\text{Ti}_3\text{C}_2\text{T}_x$  MXene and MXene-derived  $\text{TiO}_2$  microparticles (thermal annealing condition: 0 min at  $550^\circ\text{C}$ ) are reported in Supplementary Fig. 4. The  $\text{Ti}_3\text{C}_2\text{T}_x$  MXene appears as a black powder absorbing in the visible range from 300 to 700 nm. In comparison, the MXene-derived  $\text{TiO}_2$  microparticles appear gray with an absorption edge at 400 nm, as expected for  $\text{TiO}_2$ , and a weak absorption in the visible range due to unconverted MXene.

X-ray photoelectron spectroscopy (XPS) was performed to study the surface composition and chemical states of the  $\text{Ti}_3\text{C}_2\text{T}_x$  MXene and MXene-derived  $\text{TiO}_2$  microparticles (thermal annealing condition: 0 min at  $550^\circ\text{C}$ ). The survey spectra reported in Supplementary Fig. 5 indicate the presence of Ti, C, and O in the two samples, as well as F. The F peak is due to the  $\text{F}^-$  ions of the hydrofluoric acid solution used to etch the MAX phase, and it is more pronounced in the pristine sample. High-resolution XPS spectra of Ti  $2p$ , C  $1s$ , and O  $1s$  for the  $\text{Ti}_3\text{C}_2\text{T}_x$  MXene (top panels) and MXene-derived  $\text{TiO}_2$  microparticles (bottom panels) are shown in Fig. 2e (the binding energy values for all fitted peaks are reported in Supplementary Table 1). Several peaks are identified in the Ti  $2p$  XPS spectrum of the  $\text{Ti}_3\text{C}_2\text{T}_x$  MXene, consistent with previous reports<sup>47,48</sup>. In contrast, only  $\text{TiO}_2$  Ti  $2p_{3/2}$  and Ti  $2p_{1/2}$  peaks are present for the MXene-derived  $\text{TiO}_2$  microparticles. A significant difference is observed in the C  $1s$  spectra since the C-Ti-T $_x$  peak at 281.7 eV binding energy disappears for the MXene-derived  $\text{TiO}_2$  microparticles. Moreover, in the O  $1s$  spectrum of the MXene-derived  $\text{TiO}_2$  microparticles, the C-Ti-O $_x$  peak is lower than the  $\text{Ti}_3\text{C}_2\text{T}_x$  MXene, while a pronounced  $\text{TiO}_2$  peak is noted. These results confirm the successful conversion of  $\text{Ti}_3\text{C}_2\text{T}_x$  into  $\text{TiO}_2$ , in agreement with XRD and optical measurements.

Elemental mapping images of several microparticles were acquired by energy dispersive X-ray spectroscopy (EDX) to verify the deposition of the Pt layer and the surface decoration with  $\gamma\text{-Fe}_2\text{O}_3$  nanoparticles (Fig. 2f). These reveal the uniform presence of Ti, O, Pt, and Fe in all microparticles. Besides, the XRD pattern of the final sample exhibited Pt and  $\gamma\text{-Fe}_2\text{O}_3$  characteristics peaks (Supplementary Fig. 6). XPS analysis confirmed the presence of  $\text{Pt}^0$  and  $\gamma\text{-Fe}_2\text{O}_3$  on the microrobots' surface (Supplementary

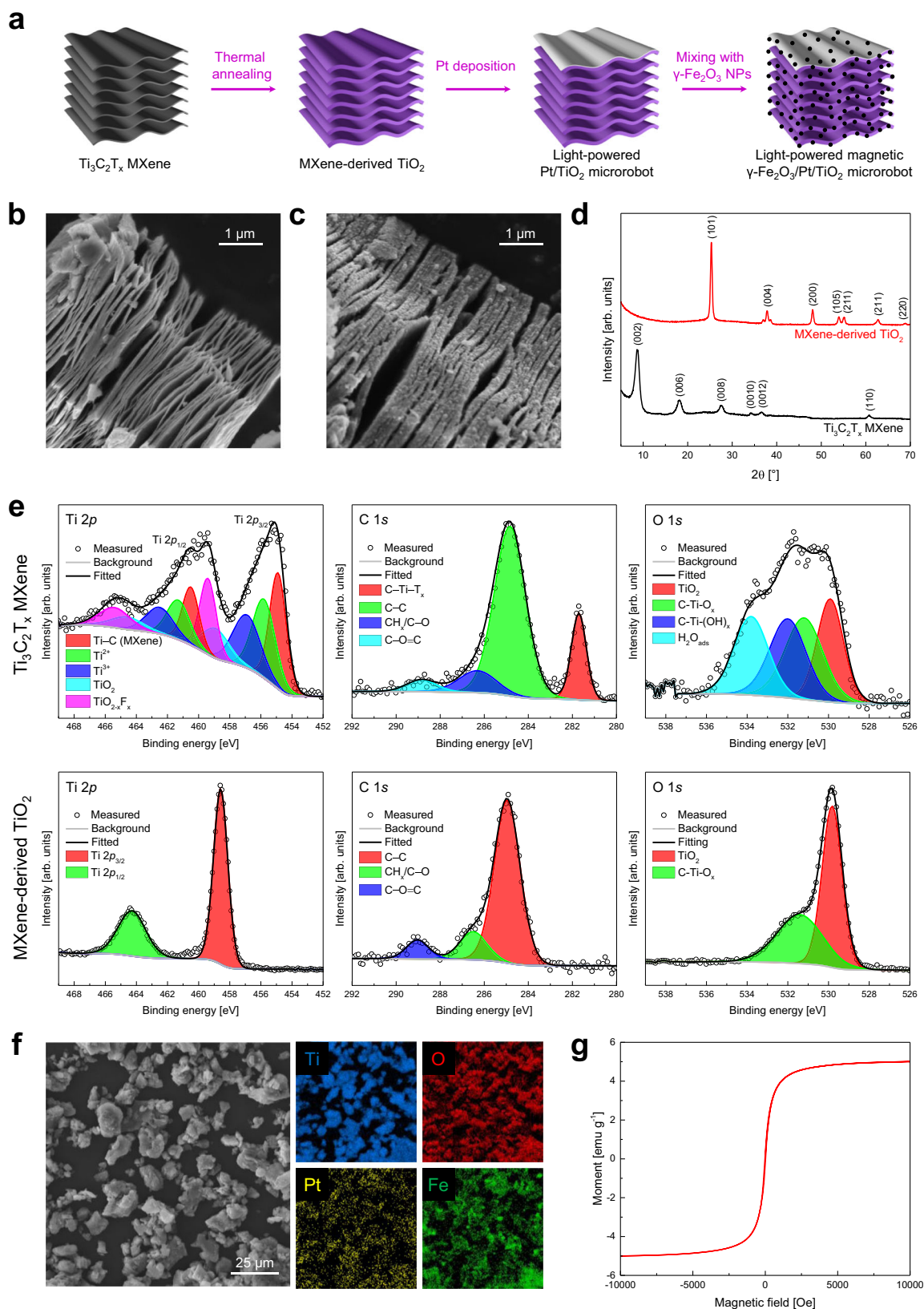


**Fig. 2** Fabrication and characterization of the MXene-derived  $\gamma\text{-Fe}_2\text{O}_3/\text{Pt}/\text{TiO}_2$  microrobots. **a** Scheme of the fabrication steps. **b**  $\text{Ti}_3\text{C}_2\text{T}_x$  MXene microparticle and **c** MXene-derived  $\gamma\text{-Fe}_2\text{O}_3/\text{Pt}/\text{TiO}_2$  microrobot (thermal annealing condition: 0 min at 550 °C) SEM images. **d** XRD patterns of  $\text{Ti}_3\text{C}_2\text{T}_x$  MXene and MXene-derived  $\text{TiO}_2$  microparticles (thermal annealing condition: 0 min at 550 °C). **e** Ti 2p, C 1s, and O 1s high-resolution XPS spectra for the  $\text{Ti}_3\text{C}_2\text{T}_x$  MXene and MXene-derived  $\text{TiO}_2$  microparticles (thermal annealing condition: 0 min at 550 °C). **f** Elemental mapping images for Ti, O, Pt, and Fe and **g** VSM curve of MXene-derived  $\gamma\text{-Fe}_2\text{O}_3/\text{Pt}/\text{TiO}_2$  microrobots (thermal annealing condition: 0 min at 550 °C).

Fig. 7), further proving the successful fabrication of MXene-derived  $\gamma\text{-Fe}_2\text{O}_3/\text{Pt}/\text{TiO}_2$  microrobots. The microrobots were also characterized using a vibrating sample magnetometer (VSM) to study their magnetic properties. The measured magnetization curve in Fig. 2g displays no hysteresis with zero coercivity and remanence, pointing to a superparamagnetic behavior. Supplementary Movie 1 shows the fast magnetic collection of the microrobots in water using a neodymium magnet.

**Microrobots' motion behavior.** Proving the self-propulsion ability of the MXene-derived  $\gamma\text{-Fe}_2\text{O}_3/\text{Pt}/\text{TiO}_2$  microrobots in water under UV-light irradiation is crucial for their further utilization as autonomous platforms to catch and trap nanoplastics. Microrobots' motion was studied in water at pH 7 using an external UV-light source. It was noticed that, without the Pt layer, some MXene-derived  $\text{TiO}_2$  microparticles could move under UV-light irradiation in the presence of relatively high  $\text{H}_2\text{O}_2$  concentrations ( $>1\%$   $\text{H}_2\text{O}_2$ ) due to their asymmetric structure. However, their low speed and the required toxic  $\text{H}_2\text{O}_2$  made them less attractive than the MXene-derived  $\gamma\text{-Fe}_2\text{O}_3/\text{Pt}/\text{TiO}_2$  microrobots, whose motion did not require fuel or surfactant. Most of the observed microrobots exhibit Brownian motion in dark and autonomous motion under UV-light irradiation on the focal plane (xy plane). Figure 3a reports two frames showing the trajectories of two microrobots after 5 s in dark (left panel) and after 5 s under UV-light irradiation (right panel), while the corresponding video, including also other microrobots, is Supplementary Movie 2. They display a rapid on/off switching of motion with the UV-light, which is reflected in the quick variations of the instantaneous speed vs. time in Fig. 3b. Moreover, a remarkable deceleration is noted within a few s from the beginning of the UV-light irradiation, followed by a plateau. The motion behavior of these microrobots results from the equilibrium between the gravitational force, the buoyancy force, and the driving force of their light-powered self-propulsion, as illustrated in Fig. 3c. The driving force, in combination with the buoyancy force, is not powerful enough to overcome the gravitational force exerted on the microrobots. As a consequence, they can move only at the bottom of the vessel, like for most of the reported semiconductor-based micromotors<sup>16,25</sup>. This typical motion behavior, limited to the xy plane, will be referred to as “2D motion” in this manuscript.

On the contrary, a relevant fraction of the microrobots showed an anomalous motion behavior, which is presented in the frames reported in Fig. 3d for an on/off switching of the UV-light (the corresponding video, including also other microrobots, is Supplementary Movie 3). In the dark, these microrobots display Brownian motion and are indistinguishable from the microrobots moving in 2D. However, under UV-light irradiation, they unfocus in a few s and completely disappear within 5 s, suggesting a movement in the upward direction. This phenomenon is known as negative photogravitaxis, i.e., a particles' migration against gravity when irradiated vertically from the bottom of the substrate, which has been previously observed for other photochemical micromotors<sup>49–51</sup>. By turning off the UV-light, they start focusing and landing at the bottom of the microscope glass slide, being under focus within 5–10 s. A similar behavior has been noticed for visible-light-driven  $\text{TiO}_2/\text{Fe}_3\text{O}_4/\text{CdS}$  microsubmarines<sup>42</sup>. It is worth remarking that the trajectories reported in Fig. 3d are only the projections on the xy plane of the actual microrobots' trajectories in the 3D space. Figure 3e reports the instantaneous speed of the two microrobots vs. time. While the speed increases quickly by turning on the UV-light, it decreases slowly by turning it off. This is due to the fact that, during microrobots' landing, they show a displacement. Such

passive motion is then translated into a decreasing speed. It was also noted that when turning on the UV-light, most of these microrobots initially undergo a self-orientation, reaching a stand-up position within 100 ms, as shown in Fig. 3f, before starting unfocusing (Supplementary Movie 4). This is ascribed to the powerful driving force exerted on the microrobots, which, together with the buoyancy force, prevails over the gravitational force, inducing their self-orientation and motion with six degrees of freedom, as illustrated in Fig. 3g. This peculiar motion behavior in the xyz space will be referred to as “3D motion”.

Microrobots' average speed under UV-light irradiation was estimated from more than 100 different microrobots' trajectories. The measured speed values are reported in the histograms in Fig. 4a for the 2D motion (top panel), i.e., for microrobots moving only on the xy plane, and 3D motion (bottom panel), i.e., for microrobots moving in the xyz space. It is noted that 60% of the analyzed microrobots move in 2D, while 40% move in 3D. The average speed values for the two motion behaviors were obtained by fitting the data with a Gaussian function. Microrobots moving in 2D have an average speed of  $9 \pm 4 \mu\text{m s}^{-1}$ , while those moving in 3D have a higher speed of  $16 \pm 8 \mu\text{m s}^{-1}$ . The real speed of the latter is even higher since it was calculated (as it is standard in this field) only for their projections on the xy plane. Nevertheless, the speed of microrobots moving in 2D is still comparable to or higher than the other fuel-free semiconductor-based micromotors<sup>25–28,41,42</sup>, which is consistent with the large electrochemical potential difference between MXene-derived  $\text{TiO}_2$  microparticles and Pt electrodes measured by Tafel experiments in ultra-pure water (Supplementary Fig. 8).

To explain the difference in speed between the microrobots moving in 2D and in 3D, which in turn is responsible for the two observed motion behaviors, some considerations regarding the motion mechanism of the microrobots are necessary. The general motion mechanism of light-powered Pt/ $\text{TiO}_2$  Janus micromotors is represented in Fig. 4b.  $\text{TiO}_2$  is an *n*-type semiconductor with a bandgap of 3.2 eV; consequently, it absorbs light in the UV region. Upon exposure to UV-light, electrons are promoted to the  $\text{TiO}_2$  conduction band, leaving holes in the valence band. The metal/semiconductor Schottky junction at the Pt/ $\text{TiO}_2$  interfaces facilitates charge separation. Electrons transferred from the  $\text{TiO}_2$  conduction band to Pt and holes left in  $\text{TiO}_2$  decompose water according to the reactions reported in Fig. 4b. In particular, the protons ( $\text{H}^+$ ) generated at the  $\text{TiO}_2$  side are consumed at the Pt side to produce  $\text{H}_2$ , establishing an  $\text{H}^+$  concentration gradient and, thus, a local electric field. This, in turn, drives Pt/ $\text{TiO}_2$  micromotors' motion via a self-electrophoretic mechanism with  $\text{TiO}_2$  as the forward side<sup>52</sup>. In this context, the Pt coating plays a key role. Pt deposition can be affected by the morphology of the underlying semiconductor microparticle. In fact, for UV-light-powered Pt/ $\text{ZnO}$  Janus micromotors, it has been demonstrated that a smooth  $\text{ZnO}$  microparticle results in a continuous Pt coating and the fuel-free motion ability, while a rough  $\text{ZnO}$  microparticle leads to a discontinuous Pt coating which requires  $\text{H}_2\text{O}_2$  fuel for the autonomous propulsion<sup>27</sup>. Similarly, smooth  $\text{TiO}_2$  microparticles coated by a continuous Pt layer exhibited a higher speed under UV-light-irradiation in  $\text{H}_2\text{O}_2$  than rough ones<sup>53</sup>. Moreover, it has been shown that transforming a continuous Pt film on  $\text{SiO}_2$  microspheres into discrete Pt nanoparticles via thermal annealing causes an  $\sim 80\%$  decrease in their self-electrophoretic speed due to the lower electric field or fluid flow generated by the discontinuous Pt coating<sup>54</sup>.

Contrarily to conventional semiconductor microparticles, the MXene-derived  $\text{TiO}_2$  microparticles present an intrinsic asymmetry owing to the formerly MXene multi-layered structure. By ideally assuming these microparticles as cubes/parallelepipeds formed by several adjacent layers, it is observed that four faces out

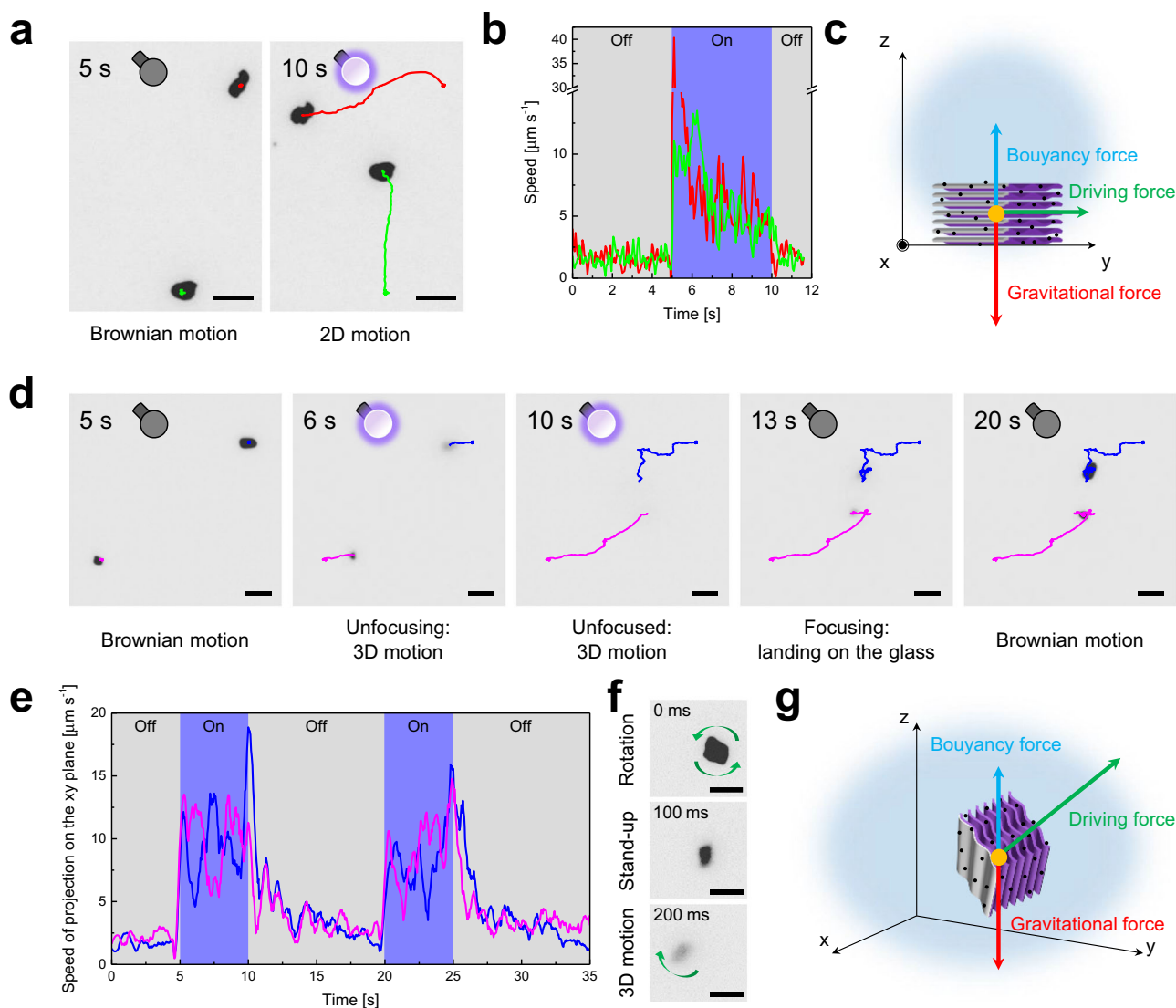


**Fig. 3** Motion behavior of the MXene-derived  $\gamma\text{-Fe}_2\text{O}_3/\text{Pt}/\text{TiO}_2$  microrobots in water under light irradiation. **a** Representative trajectories of the MXene-derived  $\gamma\text{-Fe}_2\text{O}_3/\text{Pt}/\text{TiO}_2$  microrobots (thermal annealing condition: 0 min at 550 °C) moving on the xy plane (2D motion) in fuel-free water at pH 7 in the absence and presence of UV-light irradiation, **b** their corresponding instantaneous speed vs. time, and **c** force analysis. **d** Representative trajectories of the MXene-derived  $\gamma\text{-Fe}_2\text{O}_3/\text{Pt}/\text{TiO}_2$  microrobots (thermal annealing condition: 0 min at 550 °C) moving in the xyz space (3D motion) in fuel-free water at pH 7 in the absence and presence of UV-light irradiation, **e** their corresponding instantaneous speed vs. time (trajectories and speeds are the projections of the actual microrobots' trajectories and speeds on the xy plane), **f** representative self-orientation by switching on the UV-light irradiation, and **g** force analysis. Scale bars are 10  $\mu\text{m}$ .

of six are layered and discontinuous. At the same time, the remaining two are flat and continuous. Pt deposition by sputtering technique is conducted on substrates placed in front of the Pt target. These substrates consist of microscope glass slides on which a suspension of MXene-derived  $\text{TiO}_2$  microparticles is dropped and dried overnight to form a monolayer of particles. During this preliminary preparation step, it can be assumed that the particles randomly deposit on the glass slides. So, in the ideal case, there is a probability of ~67% and ~33% to have one of the multi-layered or flat faces like the one exposed to the Pt target, as depicted in Fig. 4c. These probabilities are in good agreement with the relative frequency of 2D and 3D moving microrobots (60 and 40%, respectively), suggesting that a continuous Pt deposition on the flat side of the MXene-derived  $\text{TiO}_2$  microparticle may be the origin of the higher speed and stronger propulsive force of the resulting microrobots. This powerful driving force, combined with the buoyancy, overcomes the gravitational force and unlocks

the microrobots' movement in the upward direction, leading to their 3D motion ability. To corroborate this conclusion, a 2D simulation of the  $\text{H}_2$  production from the Pt side by consuming the protons generated under UV-light irradiation at the  $\text{TiO}_2$  side was performed for the two configurations illustrated in Fig. 4c. The simulated  $\text{H}_2$  concentration spatial distribution after 0.1 s irradiation is shown in Fig. 4d. The continuous Pt coating on the flat side of the MXene-derived  $\text{TiO}_2$  microparticle produces more  $\text{H}_2$  compared to the discontinuous Pt coating on the multi-layered side, reflecting a larger  $\text{H}^+$  concentration gradient and, so, a higher speed and 3D motion ability. This conclusion is consistent with the previously reported stronger propulsion for microrobots coated by a continuous Pt layer<sup>27,53,54</sup>.

**Nanoplastics' capture.** As representatives for nanoplastic debris, carboxylated polystyrene nanoparticles with a diameter of 50 nm

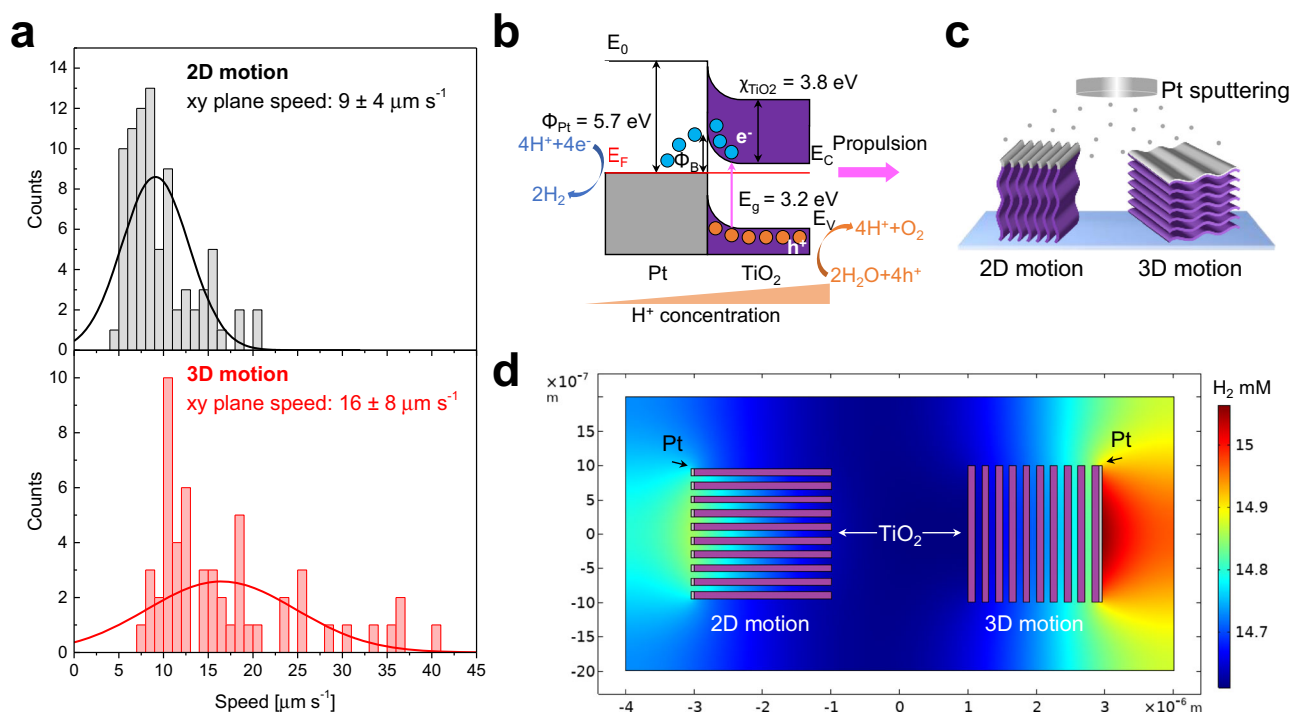


**Fig. 4** Analysis of the MXene-derived  $\gamma\text{-Fe}_2\text{O}_3/\text{Pt}/\text{TiO}_2$  microrobots' 2D and 3D motion. **a** Speed distributions of the MXene-derived  $\gamma\text{-Fe}_2\text{O}_3/\text{Pt}/\text{TiO}_2$  microrobots (thermal annealing condition: 0 min at  $550^\circ\text{C}$ ) showing 2D and 3D motion in water at pH 7 under UV-light irradiation. **b** Scheme of the general motion mechanism of Pt/ $\text{TiO}_2$  microrobots ( $E_0$  is the vacuum level,  $E_F$  is the Fermi level,  $\Phi_{\text{Pt}}$  is Pt work function,  $\Phi_{\text{B}}$  is the Schottky barrier height,  $E_C$ ,  $E_V$ ,  $E_g$ , and  $\chi_{\text{TiO}_2}$  are  $\text{TiO}_2$  conduction and valence band levels, optical bandgap, and electron affinity). **c** Scheme of the two MXene-derived  $\gamma\text{-Fe}_2\text{O}_3/\text{Pt}/\text{TiO}_2$  microrobots' configurations originated from the MXene-derived  $\text{TiO}_2$  microparticles' multi-layered structure and orientation with respect to the Pt target during Pt deposition. **d** Numerical simulation of the  $\text{H}_2$  concentration spatial distribution produced in 0.1 s for the cross-section of the two configurations.

were used. The concentration of nanoplastics in water samples was determined by NTA. This method allows measuring the size distribution and concentration of nanoparticles in environmental, biological, and food samples<sup>55</sup>. In particular, NTA has been used to estimate the concentration of nanoplastics in water samples and the release of nanoplastics as a result of (micro)plastics' degradation<sup>11</sup>. In addition, it has been employed to measure the diffusion coefficient of autonomous nanomotors<sup>56,57</sup>. The working principle of NTA is schematically illustrated in Fig. 5a. A laser beam passes through the nanoplastics' suspension in the sample's chamber. The light scattered by the nanoplastics is observed and recorded using a microscope equipped with a camera. A software tracks the nanoplastics' Brownian motion at a fixed temperature and, using the Stokes-Einstein equation, calculates their hydrodynamic diameters.

Figure 5b shows the average size distribution of the nanoplastics' suspension after a dilution by a factor  $5 \times 10^4$ , obtained through NTA. An average size of 50 nm is noted, as expected. The area of the size distribution yields the concentration of nanoplastics, which is  $\sim 6 \times 10^9$  nanoplastics  $\text{ml}^{-1}$  after the dilution. Based on the information provided by the supplier of the carboxylated polystyrene nanoparticles' suspension and polystyrene density ( $1.05 \text{ g cm}^{-3}$ ), nanoplastics' concentration before the dilution should be  $1.5 \times 10^{14}$  nanoplastics  $\text{ml}^{-1}$  (Supplementary Discussion 1). After the dilution, the nanoplastics' concentration should be  $3 \times 10^9$  nanoplastics  $\text{ml}^{-1}$ . This value is in good agreement with the nanoplastics' concentration measured through NTA, demonstrating the reliability of the proposed methodology. Before the nanoplastics' capture experiments with the microrobots, the optimal nanoplastics' concentration range for NTA was determined by serial dilution. Frames from the

videos recorded for the various nanoplastics' suspensions are shown in Fig. 5c (the videos are reported in Supplementary Movie 5). Nanoplastics are visualized as bright spots on a dark background. It is noticed that the number of the spots decreases by increasing the dilution factor (DF). The corresponding calibration curve is displayed in Fig. 5d. The nanoplastics' concentration ( $\sim 6 \times 10^9 \div 2 \times 10^7$  nanoplastics  $\text{ml}^{-1}$ ) is linear over a wide range of dilutions ( $5 \times 10^4 \div 1 \times 10^7$ ).

The proposed nanoplastics' remediation strategy is represented in Fig. 6a. The MXene-derived  $\gamma\text{-Fe}_2\text{O}_3/\text{Pt}/\text{TiO}_2$  microrobots accelerate nanoplastics' trapping thanks to the powerful self-propulsion ability under light irradiation and an engineered electrostatic attraction. Then, the microrobots and the trapped nanoplastics are collected magnetically and separated from the treated water. The electrostatic attraction has already been addressed as an effective strategy for capturing polymer chains and microplastics<sup>15,25</sup>. Therefore, the Zeta potentials of the microrobots and nanoplastics were measured at different pH to maximize their electrostatic attraction (Fig. 6b). The nanoplastics used in this work are negatively charged due to the surface carboxylic groups. At pH 3, their Zeta potential is  $-60 \text{ mV}$ . Contrarily, the microrobots are only slightly positive at pH 7, displaying a Zeta potential of  $+12 \text{ mV}$ . This increases up to  $+43 \text{ mV}$  at pH 3. Therefore, all nanoplastics capture experiments have been conducted in pH 3 water. Microrobots' motility in water at pH 3 was studied. About 13% of the recorded microrobots show the 3D motion, although at a lower average speed than pH 7 (Supplementary Fig. 9). Also, the speed of the 2D motion decreases significantly. This behavior is explained by the higher ionic strength of water at pH 3 or the lower microrobots' photochemical activity<sup>58</sup>. In addition, the attraction

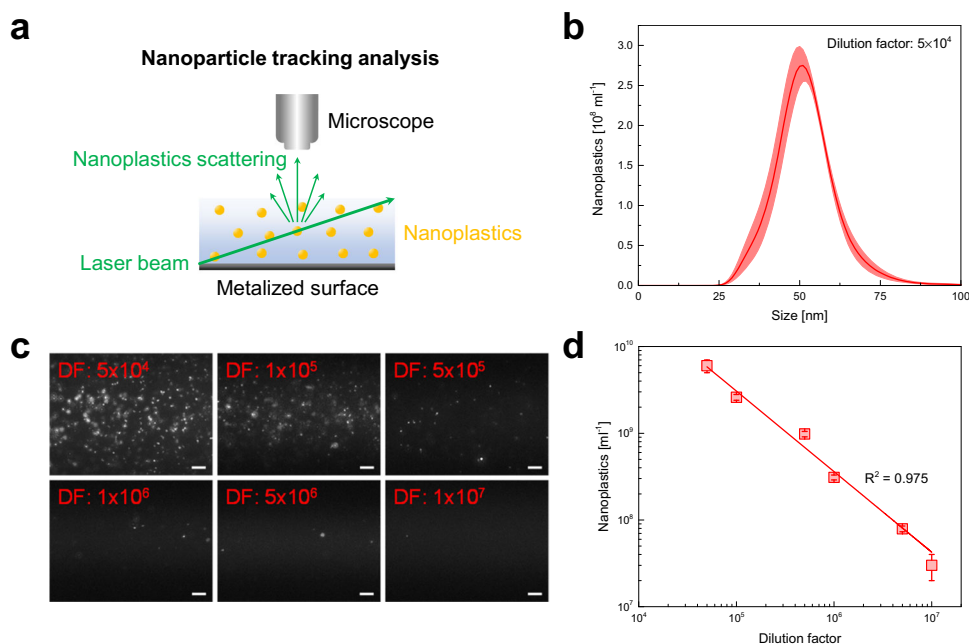


**Fig. 5 Nanoparticle tracking analysis (NTA).** **a** Scheme of the NTA working principle. **b** Size distribution of the nanoplastics' suspension (carboxylated polystyrene nanoparticles in water) after the dilution by a factor  $5 \times 10^4$  measured by NTA. The shaded region replaces the discrete error bars calculated as the standard error for  $n = 3$  independent replicates. **c** Frames of the videos of nanoplastics' suspensions after serial dilution and **d** the corresponding calibration curve showing the linear range for NTA. Scale bars are  $10 \mu\text{m}$ . Error bars represent the standard deviation,  $n = 3$  independent replicates.

between the positively charged microrobots and the negatively charged glass slide may contribute to slowing down the microrobots, which more often are stuck to the substrate.

Figure 6c reports the SEM images of a microrobot after exposure to the nanoplastics' suspension before dilution for 1 min under UV-light irradiation. Nanoplastics are noticed on the microrobot's surface, including the slits between the formerly MXene's multi-layer stacks, demonstrating the efficacy of the multi-layered design and electrostatic trapping. A quantitative study of nanoplastics' capture for different treatment durations (1, 3, and 5 min) was conducted through the NTA. To exploit the entire linear range, the initial nanoplastics' concentration was set to  $\sim 6 \times 10^9$  nanoplastics  $\text{ml}^{-1}$ .  $\gamma\text{-Fe}_2\text{O}_3/\text{Ti}_3\text{C}_2\text{T}_x$  MXene microparticles served as a reference to better evaluate the contribution of microrobots' self-propulsion to the nanoplastics' capture. Figure 6d shows frames from the videos of the nanoplastics' suspensions after the treatments with MXene and microrobots (the videos are reported in Supplementary Movie 6). At the same time, the measured nanoplastics' concentration values are shown in Fig. 6e. Most nanoplastics are still present even after the more prolonged treatment with the MXene microparticles. In particular, after 5 min-long treatment, the concentration of nanoplastics decreased from  $(6 \pm 1) \times 10^9$  to  $(3 \pm 1) \times 10^9$  nanoplastics  $\text{ml}^{-1}$ , which corresponds to a nanoplastics' capture efficiency of 50%. It is worth noting that the scattering of the nanoplastics increased after the treatment, which is reflected in the brighter spots in Fig. 6d for 1, 3, and 5 min. On the contrary, the microrobots catch 97% of the nanoplastics within 1 min, leaving only  $(4.4 \pm 0.6) \times 10^7$  nanoplastics  $\text{ml}^{-1}$  in the water sample after 5 min. In fact, the MXene microparticles land on the bottom of the vessel. Instead, the microrobots can capture many more nanoplastics due to their active motion. Control experiments using the microrobots without UV-light irradiation, i.e., in the static condition, revealed a trend similar to the MXene microparticles (Supplementary Fig. 10), further confirming the crucial contribution of microrobots' self-propulsion to the nanoplastics' capture process.

The microrobots' removal capacity  $q_t$  [ $\text{mg g}^{-1}$ ] was calculated and plotted in Supplementary Fig. 11 to allow a straightforward comparison with "conventional" materials tested under similar conditions in recent studies. The microrobots reached a  $q_t$  of  $0.5 \pm 0.1 \text{ mg g}^{-1}$  within 1 min treatment. This value is close to that reported for other materials, such as granular activated carbon ( $\sim 0.3\text{--}0.7 \text{ mg g}^{-1}$  after 15 min)<sup>59</sup>, cellulose fibers ( $0.8\text{--}0.86 \text{ mg g}^{-1}$  after 5–120 min)<sup>60</sup>, and untreated coffee grains ( $>2 \text{ mg g}^{-1}$  after 5 min)<sup>61</sup>, despite having a larger surface area and being utilized under external agitation.

The microrobots' reusability has been tested by several nanoplastics' capture and release cycles (Supplementary Fig. 12). It was found that they could be reused many times as their capture ability decreased slightly after each run.

**Nanoplastics' detection.** The microrobots' rapid nanoplastics collection ability inspired their use as self-propelled platforms for fast nanoplastics' preconcentration and further detection through the EIS technique as a cheap, fast, and portable alternative to NTA. The measurement involves a conventional three-electrode electrochemical cell comprising working, reference, and counter electrodes connected to a potentiostat and a redox probe in the electrolyte solution. A small-amplitude sinusoidal voltage is applied to the working electrode at several frequencies. The fit of the EIS spectrum based on an equivalent circuit model allows the determination of the circuit parameters. By monitoring these parameters, EIS can be used to sensitively detect impedance variations at the electrolyte/electrode interface caused by the adsorption of molecules or particles<sup>62</sup>.

Here, the three-electrode setup has been replaced with commercial SPEs, which have the advantage of miniaturization and portability, low cost, and low sample volume<sup>63</sup>. To demonstrate the importance of nanoplastics' preconcentration for sensing, the EIS spectra of an SPE in the absence and presence of nanoplastics ( $\sim 10^{12}$  nanoplastics  $\text{ml}^{-1}$ ) were first measured using  $\text{Fe}(\text{CN})_6^{4-/3-}$  as the redox probe. Figure 7a reports the obtained Nyquist plots, showing the impedance real and



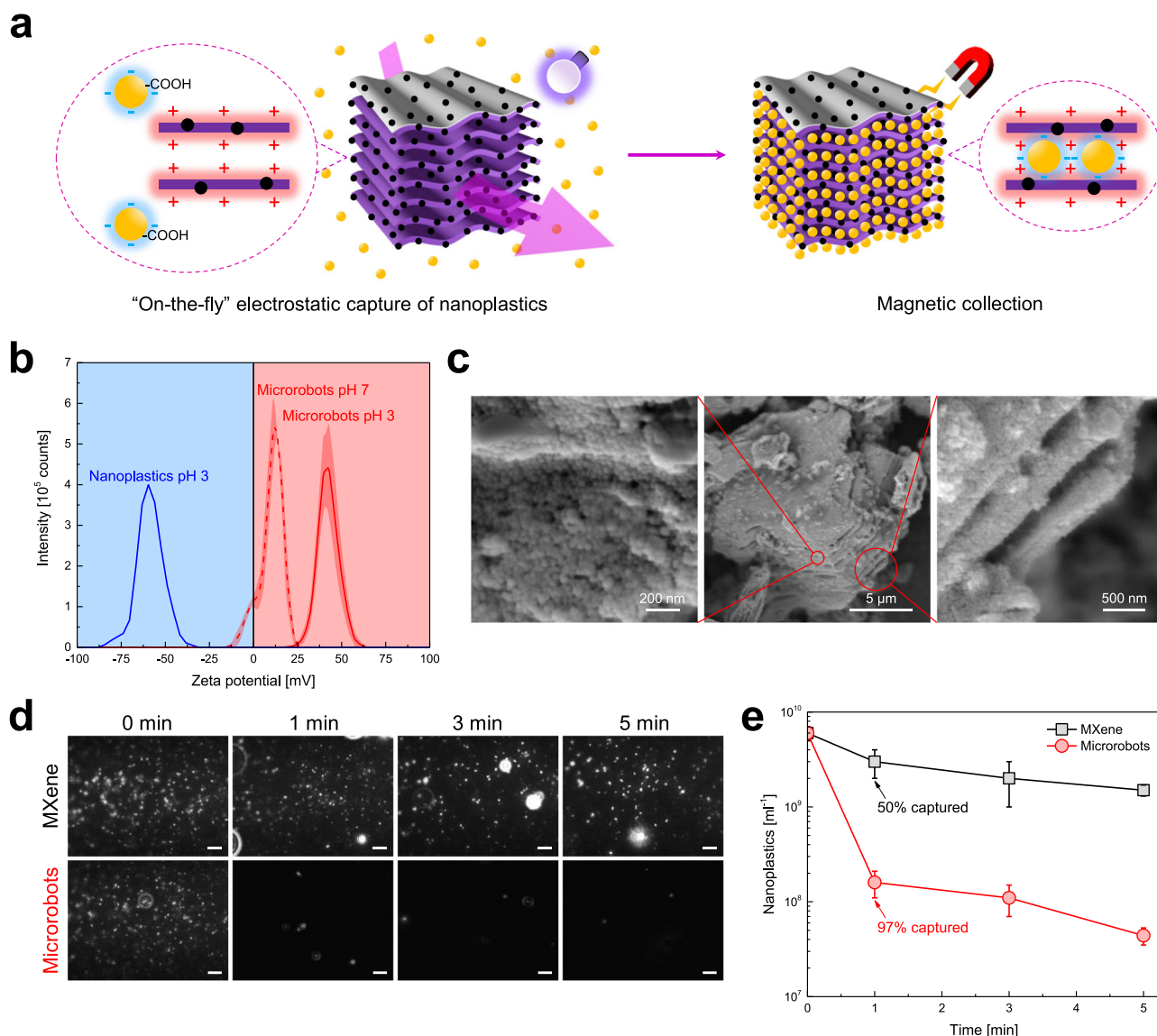


**Fig. 6** Nanoplastics' capture by MXene-derived  $\gamma\text{-Fe}_2\text{O}_3/\text{Pt}/\text{TiO}_2$  microrobots. **a** Scheme of the nanoplastics' remediation strategy: nanoplastics are electrostatically collected by the self-propelled light-powered MXene-derived  $\gamma\text{-Fe}_2\text{O}_3/\text{Pt}/\text{TiO}_2$  microrobots and magnetically removed from the treated water using a magnetic field. **b** Zeta potential of the MXene-derived  $\gamma\text{-Fe}_2\text{O}_3/\text{Pt}/\text{TiO}_2$  microrobots (thermal annealing condition: 0 min at 550 °C) and nanoplastics in water at various pH. The shaded regions replace the discrete error bars calculated as the standard error for  $n = 3$  independent replicates. **c** SEM images of an MXene-derived  $\gamma\text{-Fe}_2\text{O}_3/\text{Pt}/\text{TiO}_2$  microrobot (thermal annealing condition: 0 min at 550 °C) after exposure to the nanoplastics suspension (capture experiment conditions: 0.75 mg ml<sup>-1</sup> microrobots,  $1.5 \times 10^{14}$  nanoplastics ml<sup>-1</sup>, water at pH 3, UV-light irradiation for 1 min, microrobots' collection using a neodymium magnet). **d** Frames of the videos of nanoplastics' suspensions after the treatments with the  $\gamma\text{-Fe}_2\text{O}_3/\text{Ti}_3\text{C}_2\text{T}_x$  MXene microparticles and MXene-derived  $\gamma\text{-Fe}_2\text{O}_3/\text{Pt}/\text{TiO}_2$  microrobots for different durations (1, 3, and 5 min) under UV-light irradiation (capture experiments conditions: 0.75 mg ml<sup>-1</sup> sample,  $6 \times 10^9$  nanoplastics ml<sup>-1</sup>, water at pH 3, samples' collection using a neodymium magnet), and **e** the corresponding nanoplastics' concentration values obtained by NTA. Scale bars are 10  $\mu$ m. Error bars represent the standard deviation,  $n = 3$  independent replicates.

imaginary parts as a function of the frequency (the corresponding Bode plots, showing impedance modulus and phase as a function of the frequency, are reported in Supplementary Fig. 13). The two curves are almost overlapped and display a small semicircle arc in the high-frequency region (left) and a straight line in the low-frequency region (right). The minor difference between these curves suggests that a bare SPE is insufficient to unambiguously discriminate a nanoplastics-contaminated water sample from a pure one.

An aqueous suspension of the microrobots with captured nanoplastics was dropped onto an SPE to perform the EIS measurement. The SPE was equipped with a magnet on the backside to accelerate the landing of the microrobots and stick

them on the working electrode area during the replacement of water with the electrolyte. The same procedure was executed for a suspension of microrobots without nanoplastics, which served as a reference. The Nyquist plots of microrobots with and without captured nanoplastics are also presented in Fig. 7a. A large semicircle is noted in both cases, while the straight line is just hinted. Nevertheless, the diameter of the semicircle in the presence of the nanoplastics is significantly greater. Such variation agrees with a previous report on the increased resistance of conductive membranes after the deposition of latex beads measured by EIS, and it is promising for nanoplastics' detection<sup>64</sup>.

Figure 7a shows the fit of the EIS spectra according to the equivalent circuit model depicted in Fig. 7b. This consists of the

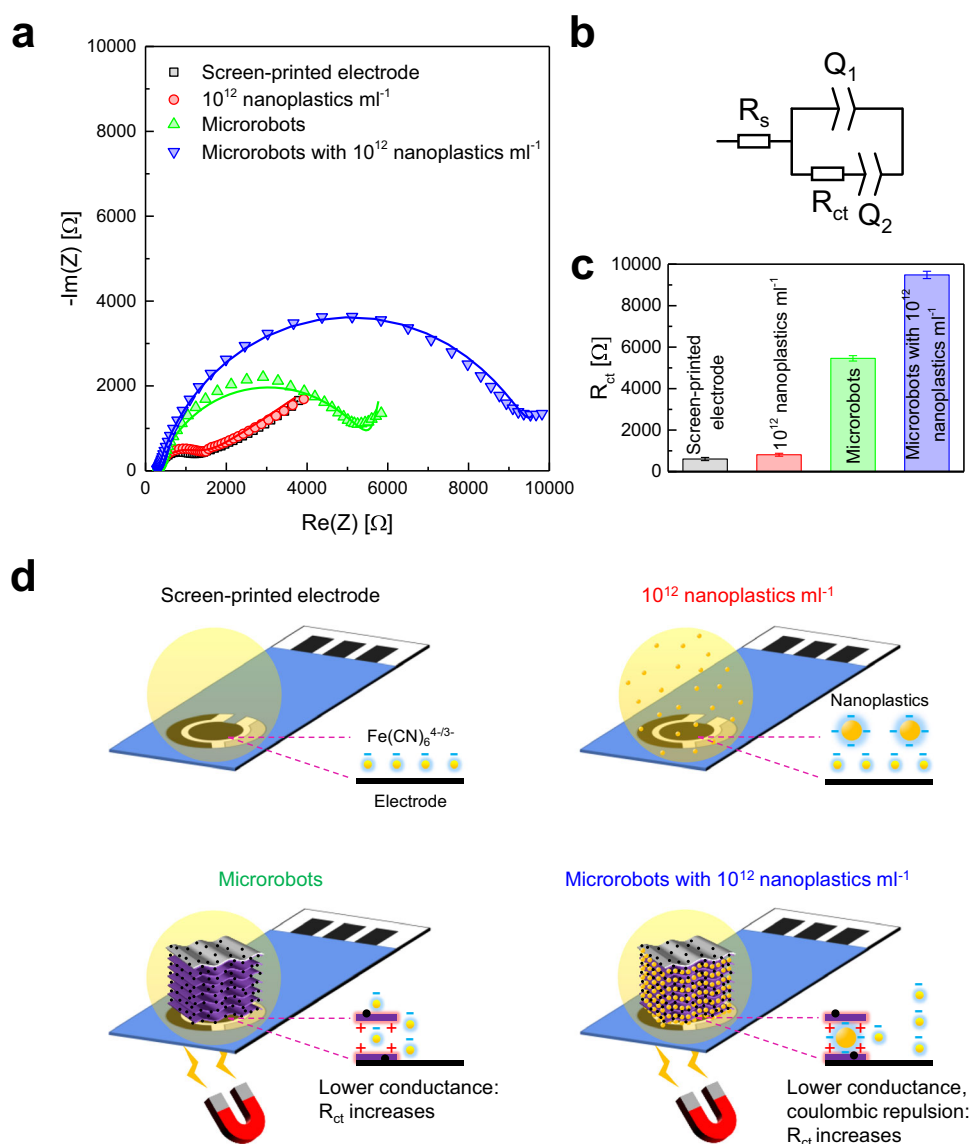


**Fig. 7 Nanoplastics' detection by electrochemical impedance spectroscopy (EIS) technique after the preconcentration with the MXene-derived  $\gamma$ - $\text{Fe}_2\text{O}_3/\text{Pt}/\text{TiO}_2$  microrobots.** **a** Nyquist plots showing the impedance real ( $\text{Re}(Z)$ ) and imaginary ( $-\text{Im}(Z)$ ) parts as a function of the frequency for a bare screen-printed electrode (SPE), an SPE exposed to  $\sim 10^{12}$  nanoplastics  $\text{ml}^{-1}$  suspension, an SPE after MXene-derived  $\gamma$ - $\text{Fe}_2\text{O}_3/\text{Pt}/\text{TiO}_2$  microrobots' (thermal annealing condition: 0 min at  $550^\circ\text{C}$ ) loading, and an SPE after loading microrobots with captured nanoplastics (capture experiment conditions:  $0.75\text{ mg ml}^{-1}$  microrobots,  $\sim 10^{12}$  nanoplastics  $\text{ml}^{-1}$ , water at pH 3, UV-light irradiation for 1 min, microrobots' collection using a neodymium magnet). The EIS measurements were performed in a  $10\text{ mM Fe}(\text{CN})_6^{4-/3-}$  aqueous solution at  $0\text{ V vs. ref.}$  with a  $10\text{ mV}$  superimposed sinusoidal root-mean-square voltage in the frequency range  $10^5 \div 10^0\text{ Hz}$ . The lines represent fits to the data. **b** Equivalent circuit model for the Nyquist plots fit: the electrolyte solution resistance ( $R_s$ ) is in series with the double-layer capacitance of the working electrode described by a constant phase element ( $Q_1$ ), which is in parallel with the charge transfer resistance at the electrolyte/electrode interface ( $R_{ct}$ ) and a second constant phase element ( $Q_2$ ). **c**  $R_{ct}$  values obtained from the Nyquist plots fit. Error bars represent the fitting error. **d** Schemes of the different EIS measurements and electrolyte/electrode interfaces representing a bare SPE, an SPE exposed to a nanoplastics' suspension, an SPE where microrobots are loaded on the working electrode, and an SPE where microrobots with captured nanoplastics are loaded on the working electrode in a  $\text{Fe}(\text{CN})_6^{4-/3-}$  solution.

electrolyte solution resistance ( $R_s$ ) in series with the double-layer capacitance of the working electrode, described through a constant phase element ( $Q_1$ ) to take into account the nonideality of the capacitor, in parallel with the charge transfer resistance at the electrolyte/electrode interface ( $R_{ct}$ ) and a second constant phase element ( $Q_2$ )<sup>65</sup>. The calculated circuit parameters are reported in Supplementary Table 2. Among all parameters, the most significant variations are observed for  $R_{ct}$ , which corresponds to the diameter of the semicircle in the Nyquist plot. Figure 7c displays the calculated  $R_{ct}$  values. A negligible increase in  $R_{ct}$  is observed for the SPE upon exposure to the nanoplastics'

suspension. The  $R_{ct}$  significantly rises after microrobots loading onto the SPE and almost doubles for microrobots with nanoplastics. This observation is consistent with transient photocurrent response measurements, showing a microrobots' photocurrent decrease after capturing nanoplastics (Supplementary Fig. 14).

The scheme in Fig. 7d allows to better understand the impedimetric behaviors of the samples. Since the nanoplastics are suspended in the solution, the electrolyte/SPE interface remains unchanged. Hence, there is only a tiny difference in the impedance of the bare SPE with and without nanoplastics. The

presence of the microrobots leads to a notable increase of the SPE's  $R_{ct}$  due to the low conductivity of the semiconducting  $TiO_2$ , which represents the main constituent of the microrobots<sup>66</sup>. This behavior has also been observed after  $TiO_2$  loading on FTO electrodes<sup>67</sup>. The  $R_{ct}$  further rises due to the lower microrobots' conductance in consequence of the inclusion of a large quantity of non-conducting polystyrene nanoparticles<sup>68</sup>. Additionally, nanoplastics' capture results in the neutralization of microrobots' positive surface charge and, thus, the Coulomb repulsion of the redox probe ions ( $Fe(CN)_6^{4-/3-}$ ), as demonstrated by the microrobots' Zeta potential decrease ( $+43 \rightarrow -1$  eV) after nanoplastics' capture (Supplementary Fig. 15). This mechanism, similar to the one at the base of DNA hybridization sensors, contributed to the  $R_{ct}$  increase<sup>62</sup>.

The method's reliability has been verified by measuring the impedance of microrobots exposed to different nanoplastics' concentrations ( $\sim 10^6$  and  $10^{14}$  nanoplastics  $ml^{-1}$ ). Supplementary Fig. 16 shows the recorded Nyquist and Bode plots, whose fitting parameters are reported in Supplementary Table 2. The  $R_{ct}$  for the bare microrobots is similar to microrobots with  $10^6$  nanoplastics  $ml^{-1}$ , suggesting that this low concentration can not produce a detectable impedance variation. On the other hand, a remarkable increase of the  $R_{ct}$  ( $\sim 18000 \Omega$ ) was obtained for the microrobots with  $10^{14}$  nanoplastics  $ml^{-1}$ , corroborating the consistency of the proposed sensing strategy.

On these bases, the microrobots quickly accumulate nanoplastics in water and allow determining their presence at concentrations higher than  $10^6$  nanoplastics  $ml^{-1}$  through impedance measurements. The rapidity and efficiency of nanoplastics' preconcentration and EIS measurement, in combination with the low cost and compactness of the SPEs, hold promise for the "on-site" nanoplastics' sensing in wastewater.

In conclusion, an efficient strategy for removing and detecting nanoplastics in water is presented based on innovative self-propelled light-powered magnetic MXene-derived microrobots.  $\gamma-Fe_2O_3/Pt/TiO_2$  microrobots were prepared by simple thermal annealing in air of exfoliated  $Ti_3C_2T_x$  MXene microparticles, followed by the deposition of a Pt layer and the surface decoration with magnetic  $\gamma-Fe_2O_3$  nanoparticles. The duration of the annealing process was optimized to preserve the characteristic multi-layered structure of MXenes. The microrobots showed a powerful motion in fuel-free water under UV-light irradiation with quick on/off switching. The Pt deposition on the flat sides of the MXene-derived  $TiO_2$  microparticles rather than on the multi-layered sides was identified as the reason for the observed higher speed and negative photogravitactic behavior, resulting in the 3D movement of the microrobots, in agreement with numerical simulations. This result proves that a continuous Pt coating generates a stronger micro/nanorobots' propulsion than a discontinuous one. The ability of microrobots to trap nanoplastics was evaluated through nanoplastics' capture experiments under UV-light irradiation using carboxylated polystyrene beads (50 nm in size) as a model for nanoplastics in water. SEM analysis confirmed the trapping of nanoplastics on the microrobots' surface, including the slits between the formerly MXene's multi-layer stacks. Compared to the static MXene microparticles, the microrobots demonstrated a superior capture efficiency (97% vs. 50% in 1 min), as confirmed by NTA, due to their fast active motion and tailored Zeta potential to attract the oppositely charged nanoplastics. The superparamagnetic behavior of the microrobots allowed their facile collection from the treated water. Owing to their rapid and excellent nanoplastics' capture capability, the microrobots were employed as self-motile platforms for the preconcentration and successive electrochemical detection of nanoplastics using low-cost SPEs by the EIS technique. Transferring the self-propulsion, photocatalytic,

magnetic, and pH-programmable surface charge properties of the microrobots to larger surface area materials would significantly enhance the nanoplastics' capture efficiency and, in principle, reduce the preconcentration time and improve the electrochemical sensor's sensitivity. This study lays the basis for the "on-site" screening of nanoplastics in wastewater. The multi-layered design of the microrobots is also promising for the removal and subsequent photocatalytic degradation of other organic pollutants in water.

## Methods

**Materials and reagents.** Exfoliated  $Ti_3C_2T_x$  MXene was purchased from Laizhou Kai Kai Ceramic Materials Co. Ltd (Hong Kong S.A.R.). Calcium chloride ( $CaCl_2$ ,  $\geq 98\%$ ), iron sulfate heptahydrate ( $FeSO_4 \cdot 7H_2O$ , ACS reagent  $\geq 99\%$ ), ammonium hydroxide ( $NH_4OH$ , 25%  $NH_3$  in  $H_2O$ ), potassium hexacyanoferrate(III) ( $K_3Fe(CN)_6$ , ACS reagent  $\geq 99\%$ ), and indium tin oxide-coated glass slides (ITO,  $75 \times 25 \times 1.1$  mm<sup>3</sup>,  $8-12 \Omega$  sq<sup>-1</sup> surface resistivity) were purchased from Sigma-Aldrich (Merck, Germany). Iron chloride hexahydrate ( $FeCl_3 \cdot 6H_2O$ , 97%) was purchased from Alfa Aesar (Thermo Fisher Scientific, US). Pt target was purchased from Neyco (France). Carboxylated polystyrene nanoparticles (1% solid content in 5 ml water, corresponding to 10 mg  $ml^{-1}$ , 50 nm in size) were purchased from Degradex (Phosphorex, US). ET077-40 SPEs (50  $\times$  13 mm<sup>2</sup>, 3 mm diameter disk working electrode, graphitic carbon powder working and auxiliary electrodes, Ag/AgCl pellet reference electrode) were purchased from Zensor (Taiwan).

**Fabrication of MXene-derived Pt/ $TiO_2$  microrobots.** Exfoliated  $Ti_3C_2T_x$  MXene microparticles were transformed into  $TiO_2$  microparticles by a thermal annealing process conducted in a tubular furnace in air with a heating rate of  $10 \text{ }^\circ\text{C min}^{-1}$  up to  $550 \text{ }^\circ\text{C}$ . To preserve the accordion-like structure of the MXene, the influence of the thermal annealing process duration (0, 30, 60, and 120 min) on the morphological and structural properties of the resulting  $TiO_2$  microparticles was investigated. To fabricate MXene-derived Pt/ $TiO_2$  microrobots, a suspension of the optimal (thermal annealing condition: 0 min at  $550 \text{ }^\circ\text{C}$ ) MXene-derived  $TiO_2$  microparticles ( $5 \text{ mg ml}^{-1}$ ) was prepared using ultra-pure water (18 M $\Omega$  cm), dropped on glass slides, and dried overnight. Then, a Pt layer (50 nm) was asymmetrically deposited on the microparticles using a Leica EM ACE600 high vacuum sputter coater. The obtained MXene-derived Pt/ $TiO_2$  microrobots were detached from the glass slides through a scalpel.

**Synthesis of  $\gamma-Fe_2O_3$  nanoparticles for microrobots' surface decoration.** To synthesize magnetic  $\gamma-Fe_2O_3$  nanoparticles, an aqueous solution containing  $FeSO_4 \cdot 7H_2O$  and  $FeCl_3 \cdot 6H_2O$  (molar ratio 1:1) was stirred for 15 min at  $60 \text{ }^\circ\text{C}$ .  $NH_4OH$  was added dropwise until pH 11 was reached and further stirred for 15 min at  $60 \text{ }^\circ\text{C}$ . The as-synthesized  $\gamma-Fe_2O_3$  nanoparticles were washed two times in ultra-pure water and ethanol, and dried overnight.

The decoration of the microrobots with  $\gamma-Fe_2O_3$  nanoparticles was carried out by adding 1 mg of the nanoparticles to a 2 ml solution of ultra-pure water and ethanol (volume ratio 1:1), followed by sonication for 30 s. 10 mg microrobots were added to the solution (microrobots to nanoparticles ratio 1:10) and stirred for 1 h at room temperature. Finally, MXene-derived  $\gamma-Fe_2O_3/Pt/TiO_2$  microrobots were magnetically collected using a neodymium magnet, washed two times in ultra-pure water and ethanol, and dried overnight. The same procedure was used to prepare  $\gamma-Fe_2O_3/Ti_3C_2T_x$  MXene microparticles used as a reference in nanoplastics' capture experiments.

**Characterization techniques.** Surface morphology and elemental composition were characterized by a TESCAN MIRA3 XMU SEM equipped with an Oxford Instruments energy dispersive X-ray (EDX) detector. The Brunauer-Emmett-Teller (BET) specific surface area was evaluated from the adsorption data registered through a 3P micro 300 instrument in the relative pressure ( $p/p_0$ ) range of  $0.1 \div 0.3$ . Before BET measurements, samples were degassed at  $300 \text{ }^\circ\text{C}$  overnight<sup>44</sup>. The crystalline structure was determined by XRD in parallel beam mode using a Rigaku SmartLab 9 kW diffractometer equipped with a high-brightness  $Cu K\alpha$  rotating anode X-ray tube operated at 45 kV and 150 mA. Surface chemical composition was studied by XPS using a Kratos Analytical Axis Supra instrument with a monochromatic Al  $K\alpha$  (1486.7 eV) excitation source. All spectra were calibrated to the adventitious C 1s peak at 284.8 eV and fitted using CasaXPS software. The magnetic hysteresis loop was measured using a Quantum Design VersaLab cryogen-free VSM at 300 K for an applied magnetic field ranging from  $-10$  to 10 kOe at steps of  $10 \text{ Oe s}^{-1}$ . Light-absorption spectra were measured using a Jasco V-750 UV-Visible spectrophotometer equipped with an integrating sphere. Zeta potential measurements were performed in water at pH 7 and 3 using a Malvern Panalytical Zetasizer Ultra instrument.

**Microrobots' motion behavior.** The light-powered motion behavior of microrobots in water was observed and recorded using a Nikon ECLIPSE TS2R inverted microscope coupled to a BASLER acA1920-155uc digital camera. All experiments were carried out in the absence of any surfactant. A 365 nm UV LED (Cool LED

pe-100) operated at  $1600 \text{ mW cm}^{-2}$  was used as the light source to power the microrobots. Videos were recorded at 20 fps and analyzed through NIS Elements Advanced Research and Fiji software to obtain microrobots' trajectories and measure their speed.

**Tafel and transient photocurrent response measurements.** Tafel measurements were carried out using a customized photoelectrochemical setup with three LZ4-04UV00 365 nm UV LED (LedEngin Inc.) in the two-electrode configuration with  $\text{TiO}_2$  electrode or Pt electrode as working electrodes and an Ag/AgCl electrode (1 M KCl) as both reference and counter electrode. The  $\text{TiO}_2$  working electrode was prepared by dropping 100  $\mu\text{l}$  of an aqueous suspension of optimal (thermal annealing condition: 0 min at  $550^\circ\text{C}$ ) MXene-derived  $\text{TiO}_2$  microparticles ( $5 \text{ mg ml}^{-1}$ ) on an ITO substrate ( $1 \times 2 \text{ cm}^2$ ) and dried overnight. The Pt working electrode was prepared by sputtering a Pt layer (50 nm) on an ITO substrate ( $1 \times 2 \text{ cm}^2$ ). Tafel measurements were recorded at a scan rate of  $5 \text{ mV s}^{-1}$  under UV-light irradiation on the working electrodes ( $1 \times 1 \text{ cm}^2$  immersed area) in ultra-pure water using a Metrohm AUTOLAB potentiostat.

Transient photocurrent response measurements were performed in the three-electrode configuration with samples as the working electrode, a Pt wire as the counter electrode, and an Ag/AgCl electrode (1 M KCl) as the reference electrode. The working electrodes were prepared by dropping 100  $\mu\text{l}$  of an aqueous suspension of MXene-derived  $\gamma\text{-Fe}_2\text{O}_3/\text{Pt}/\text{TiO}_2$  microrobots before and after nanoplastics' capture on an ITO substrate ( $1 \times 2 \text{ cm}^2$ ) and dried overnight (capture experiments conditions:  $0.75 \text{ mg ml}^{-1}$  microrobots,  $\sim 10^{12}$  nanoplastics  $\text{ml}^{-1}$ , UV-light irradiation for 5 min, microrobots' collection using a neodymium magnet). The photocurrent was measured at 0 V vs. OCP by turning on and off the UV-light irradiation at time intervals of 10 s.

**Numerical simulation.** The numerical simulation was performed using the transport of diluted species module of the COMSOL Multiphysics software. For the simulation, the cross-section of the MXene-derived Pt/ $\text{TiO}_2$  microrobots was considered. To emulate the MXene structure, the  $\text{TiO}_2$  microparticles were designed as 10 rectangles with a size of  $100 \text{ nm} \times 2 \mu\text{m}$  and inter-distance of 100 nm, placed inside an  $8 \times 4 \mu\text{m}^2$  rectangle. Pt deposition can occur on the multi-layered side or the flat side of the  $\text{TiO}_2$  microparticles. Pt deposition on the multi-layered side was designed using  $100 \times 50 \text{ nm}^2$  rectangles attached to the  $\text{TiO}_2$  rectangles on their left side. Pt deposition on the flat side was designed using a  $50 \text{ nm} \times 2 \mu\text{m}$  rectangle attached to the last  $\text{TiO}_2$  rectangle on the right. The  $\text{H}_2$  generation at the interface between Pt and water due to the photogenerated electron-hole pairs in  $\text{TiO}_2$  was simulated by choosing water/Pt boundaries as the generation ones. To calculate  $\text{H}_2$  diffusion for 0.1 s light irradiation, an  $\text{H}_2$  diffusion coefficient in water at  $25^\circ\text{C}$  of  $5.11 \times 10^{-9} \text{ m}^2 \text{ s}^{-1}$  was used, while the photogeneration rate was set to  $1 \text{ mmol m}^{-2} \text{ s}^{-1}$ .

**Nanoparticle tracking analysis.** Carboxylated polystyrene nanoparticles (50 nm) were used as a model for nanoplastics in water. Nanoplastics' concentration measurements were performed using the Malvern Panalytical NanoSight LM10 nanoparticle tracking system. The instrument was configured with a 532 nm laser diode and sCMOS camera and  $20\times$  optical objective. The nanoplastics' suspension was diluted with ultra-pure water and injected into the NanoSight cell for analysis. NTA 3.4 software was used to capture videos of nanoplastics at a constant temperature of  $25^\circ\text{C}$  and a frame rate of 30 fps. After tracking the recorded videos under the same parameters, the software returned nanoplastics' size distribution through finite track length adjustment (FTLA) and concentration per ml.

**Nanoplastics' capture experiments.** For nanoplastics' quantification by NTA, a stock solution of nanoplastics was prepared by diluting the commercial suspension by a factor of 50000 using pH 3 water. In a typical experiment, the microrobots (0.75 mg) were added to 1 ml of nanoplastics' suspension in a UV-transparent cuvette placed inside a customized irradiation chamber and exposed to the UV-light emitted by three LZ4-04UV00 365 nm UV LEDs for different durations (1, 3, and 5 min). At the end of the treatment, microrobots were magnetically separated from the solution using a neodymium magnet. Both microrobots and the treated solutions were stored for further analyses. Each experiment has been repeated at least three times. The same experiments were performed using  $\gamma\text{-Fe}_2\text{O}_3/\text{Ti}_3\text{C}_2\text{Tx}$  MXene microparticles as a reference or the microrobots without UV-light irradiation. Additional experiments have been conducted at different nanoplastics' concentrations ( $\sim 10^6$ ,  $10^{12}$ ,  $10^{14}$  nanoplastics  $\text{ml}^{-1}$ ).

The removal capacity  $q_t$  [ $\text{mg g}^{-1}$ ] was calculated according to the following equation

$$q_t = \frac{C_0 - C_t}{m} V \quad (1)$$

where  $C_0$  and  $C_t$  [ $\text{mg ml}^{-1}$ ] are the nanoplastics' concentration at 0 min and time  $t$ , respectively,  $V$  [ml] is the volume of the solution (1 ml), and  $m$  [g] is the sample's mass ( $7.5 \times 10^{-4}$  g). Nanoplastics' concentration values measured by NTA [ $\text{ml}^{-1}$ ] were converted to nanoplastics' concentration values  $C_0$  and  $C_t$  [ $\text{mg ml}^{-1}$ ] using the estimated mass for the single nanoplastic (Supplementary Discussion 1).

For the reusability test, after each capture experiment, the microrobots were vigorously agitated in water at pH 11 for 10 min to induce the release of the captured nanoplastics.

**Electrochemical impedance spectroscopy measurements.** EIS measurements were performed at an applied potential of 0 V vs. ref. with a 10 mV superimposed sinusoidal root-mean-square voltage in the frequency range  $10^5 \div 10^0 \text{ Hz}$  in 100  $\mu\text{l}$  electrolyte solution consisting of ultra-pure water with 10 mM  $\text{K}_3\text{Fe}(\text{CN})_6$  as the redox probe, using SPEs connected to a Metrohm AUTOLAB potentiostat. Before EIS measurements with microrobots, a 100  $\mu\text{l}$  aqueous suspension of microrobots (or microrobots with captured nanoplastics) was spotted drop-by-drop on the working electrode area of the SPE. A neodymium magnet placed on the SPE backside accelerated microrobots' landing and allowed them to stay onto the SPE while replacing water with the electrolyte. The EIS experiment with nanoplastics was carried out using the MXene-derived  $\gamma\text{-Fe}_2\text{O}_3/\text{Pt}/\text{TiO}_2$  microrobots collected with a neodymium magnet after the following capture experiments:  $0.75 \text{ mg ml}^{-1}$  microrobots,  $\sim 10^6$ ,  $10^{12}$ , and  $10^{14}$  nanoplastics  $\text{ml}^{-1}$ , UV-light irradiation for 1 min. There was no exposure to UV-light during the EIS measurements.

## Data availability

The data generated in this study are provided in the manuscript or its Supplementary Information or Figshare repository (<https://doi.org/10.6084/m9.figshare.19904512>).

Received: 13 November 2021; Accepted: 3 June 2022;

Published online: 22 June 2022

## References

- MacLeod, M., Arp, H. P. H., Tekman, M. B. & Jahnke, A. The global threat from plastic pollution. *Science* **373**, 61–65 (2021).
- Nanoplastic should be better understood. *Nat. Nanotechnol.* **14**, 299 (2019).
- Thompson, R. C. et al. Lost at sea: where is all the plastic? *Science* **304**, 838 (2004).
- Gigault, J. et al. Nanoplastics are neither microplastics nor engineered nanoparticles. *Nat. Nanotechnol.* **16**, 501–507 (2021).
- Mitrano, D. M., Wick, P. & Nowack, B. Placing nanoplastics in the context of global plastic pollution. *Nat. Nanotechnol.* **16**, 491–500 (2021).
- Gigault, J. et al. Current opinion: What is a nanoplastic? *Environ. Pollut.* **235**, 1030–1034 (2018).
- Wagner, S. & Reemtsma, T. Things we know and don't know about nanoplastic in the environment. *Nat. Nanotechnol.* **14**, 300–301 (2019).
- Rummel, C. D., Jahnke, A., Gorokhova, E., Kühnel, D. & Schmitt-Jansen, M. Impacts of biofilm formation on the fate and potential effects of microplastic in the aquatic environment. *Environ. Sci. Technol. Lett.* **4**, 258–267 (2017).
- Trieborskorn, R. et al. Relevance of nano- and microplastics for freshwater ecosystems: A critical review. *TrAC - Trends Anal. Chem.* **110**, 375–392 (2019).
- Cai, H. et al. Analysis of environmental nanoplastics: Progress and challenges. *Chem. Eng. J.* **410**, 128208 (2021).
- Schwaferts, C., Niessner, R., Elsner, M. & Ivleva, N. P. Methods for the analysis of submicrometer- and nanoplastic particles in the environment. *TrAC - Trends Anal. Chem.* **112**, 52–65 (2019).
- Mitrano, D. M. et al. Synthesis of metal-doped nanoplastics and their utility to investigate fate and behaviour in complex environmental systems. *Nat. Nanotechnol.* **14**, 362–368 (2019).
- Koelmans, A. A. Proxies for nanoplastic. *Nat. Nanotechnol.* **14**, 307–308 (2019).
- Nguyen, B. et al. Separation and analysis of microplastics and nanoplastics in complex environmental samples. *Acc. Chem. Res.* **52**, 858–866 (2019).
- Sarcretti, M. et al. The remediation of nano-/microplastics from water. *Mater. Today* **48**, 38–46 (2021).
- Ussia, M. et al. Active Light-Powered Antibiofilm ZnO micromotors with chemically programmable properties. *Adv. Funct. Mater.* **31**, 2101178 (2021).
- Oral, C. M., Ussia, M. & Pumera, M. Self-propelled activated carbon micromotors for 'on-the-fly' capture of nitroaromatic explosives. *J. Phys. Chem. C* **125**, 18040–18045 (2021).
- Zhang, F. et al. ACE2 receptor-modified algae-based microrobot for removal of SARS-CoV-2 in wastewater. *J. Am. Chem. Soc.* **143**, 12194–12201 (2021).
- Patino, T. et al. Self-sensing enzyme-powered micromotors equipped with pH-responsive DNA nanoswitches. *Nano Lett.* **19**, 3440–3447 (2019).
- Pacheco, M., de la Asunción-Nadal, V., Jurado-Sánchez, B. & Escarpa, A. Engineering Janus micromotors with  $\text{WS}_2$  and affinity peptides for turn-on fluorescent sensing of bacterial lipopolysaccharides. *Biosens. Bioelectron.* **165**, 112286 (2020).
- Venugopalan, P. L., Esteban-Fernández De Ávila, B., Pal, M., Ghosh, A. & Wang, J. Fantastic voyage of nanomotors into the cell. *ACS Nano* **14**, 9423–9439 (2020).

22. Schmidt, C. K., Medina-Sánchez, M., Edmondson, R. J. & Schmidt, O. G. Engineering microrobots for targeted cancer therapies from a medical perspective. *Nat. Commun.* **11**, 5618 (2020).
23. Urso, M., Iffelsberger, C., Mayorga-Martinez, C. C. & Pumera, M. Nickel sulfide microrockets as self-propelled energy storage devices to power electronic circuits “on-demand”. *Small Methods* **5**, 2100511 (2021).
24. Ying, Y. & Pumera, M. Micro/nanomotors for water purification. *Chem. - A Eur. J.* **25**, 106–121 (2019).
25. Urso, M., Ussia, M. & Pumera, M. Breaking polymer chains with self-propelled light-controlled navigable hematite microrobots. *Adv. Funct. Mater.* **31**, 2101510 (2021).
26. Maric, T., Nasir, M. Z. M., Webster, R. D. & Pumera, M. Tailoring metal/TiO<sub>2</sub> interface to influence motion of light-activated janus micromotors. *Adv. Funct. Mater.* **30**, 1908614 (2020).
27. Pourrahimi, A. M. et al. Catalytic and light-driven ZnO/Pt janus nano/micromotors: switching of motion mechanism via interface roughness and defect tailoring at the nanoscale. *Adv. Funct. Mater.* **29**, 1–8 (2019).
28. Peng, X., Urso, M. & Pumera, M. Photo-fenton degradation of nitroaromatic explosives by light-powered hematite microrobots: when higher speed is not what we go for. *Small Methods* **5**, 2100617 (2021).
29. Villa, K. et al. Visible-light-driven single-component BiVO<sub>4</sub> micromotors with the autonomous ability for capturing microorganisms. *ACS Nano* **13**, 8135–8145 (2019).
30. Villa, K., Děkanovský, L., Plutnar, J., Kosina, J. & Pumera, M. Swarming of perovskite-Like Bi<sub>2</sub>WO<sub>6</sub> microrobots destroy textile fibers under visible light. *Adv. Funct. Mater.* **30**, 2007073 (2020).
31. Urso, M. & Pumera, M. Nano/microplastics capture and degradation by autonomous nano/microrobots: a perspective. *Adv. Funct. Mater.* **32**, 2112120 (2022).
32. Wang, L., Kaeppler, A., Fischer, D. & Simmchen, J. Photocatalytic TiO<sub>2</sub> micromotors for removal of microplastics and suspended matter. *ACS Appl. Mater. Interfaces* **11**, 32937–32944 (2019).
33. Beladi-Mousavi, S. M., Hermanová, S., Ying, Y., Plutnar, J. & Pumera, M. A maze in plastic wastes: autonomous motile photocatalytic microrobots against microplastics. *ACS Appl. Mater. Interfaces* **13**, 25102–25110 (2021).
34. Zhou, H., Mayorga-Martinez, C. C. & Pumera, M. Microplastic removal and degradation by mussel-inspired adhesive magnetic/enzymatic microrobots. *Small Methods* **5**, 2100230 (2021).
35. Ye, H. et al. Magnetically steerable iron oxides-manganese dioxide core-shell micromotors for organic and microplastic removals. *J. Colloid Interface Sci.* **588**, 510–521 (2021).
36. Gogotsi, Y. & Anasori, B. The rise of MXenes. *ACS Nano* **13**, 8491–8494 (2019).
37. Alhabeb, M. et al. Guidelines for synthesis and processing of two-dimensional titanium carbide (Ti<sub>3</sub>C<sub>2</sub>T<sub>x</sub> MXene). *Chem. Mater.* **29**, 7633–7644 (2017).
38. Dixit, F. et al. Application of MXenes for water treatment and energy-efficient desalination: A review. *J. Hazard. Mater.* **423**, 127050 (2022).
39. Khandelwal, N. & Darbha, G. K. A decade of exploring MXenes as aquatic cleaners: Covering a broad range of contaminants, current challenges and future trends. *Chemosphere* **279**, 130587 (2021).
40. Wu, Y. et al. Recent advances in transition metal carbides and nitrides (MXenes): Characteristics, environmental remediation and challenges. *Chem. Eng. J.* **418**, 129296 (2021).
41. Mayorga-Martinez, C. C., Vyskočil, J., Novotný, F. & Pumera, M. Light-driven Ti<sub>3</sub>C<sub>2</sub> MXene micromotors: self-propelled autonomous machines for photodegradation of nitroaromatic explosives. *J. Mater. Chem. A* **9**, 14904–14910 (2021).
42. Ying, Y., Plutnar, J. & Pumera, M. Six-degree-of-freedom steerable visible-light-driven microsubmarines using water as a fuel: application for explosives decontamination. *Small* **17**, 2100294 (2021).
43. Low, J., Zhang, L., Tong, T., Shen, B. & Yu, J. TiO<sub>2</sub>/MXene Ti<sub>3</sub>C<sub>2</sub> composite with excellent photocatalytic CO<sub>2</sub> reduction activity. *J. Catal.* **361**, 255–266 (2018).
44. Shahzad, A. et al. Two-dimensional Ti<sub>3</sub>C<sub>2</sub>T<sub>x</sub> MXene nanosheets for efficient copper removal from water. *ACS Sustain. Chem. Eng.* **5**, 11481–11488 (2017).
45. Uekawa, N., Ono, Y. & Kojima, T. Synthesis of gluconate modified layered titanate particles using hydrolysis reaction of Ti alkoxide and characterization of their swelling behavior and structural color. *J. Sol.-Gel Sci. Technol.* **85**, 48–58 (2018).
46. Luttrell, T. et al. Why is anatase a better photocatalyst than rutile? - Model studies on epitaxial TiO<sub>2</sub> films. *Sci. Rep.* **4**, 4043 (2015).
47. Halim, J. et al. X-ray photoelectron spectroscopy of select multi-layered transition metal carbides (MXenes). *Appl. Surf. Sci.* **362**, 406–417 (2016).
48. Ghosh, K. & Pumera, M. MXene and MoS<sub>3-x</sub> Coated 3D-printed hybrid electrode for solid-state asymmetric supercapacitor. *Small Methods* **5**, 2100451 (2021).
49. Zhou, C., Zhang, H. P., Tang, J. & Wang, W. Photochemically powered AgCl janus micromotors as a model system to understand ionic self-diffusiophoresis. *Langmuir* **34**, 3289–3295 (2018).
50. Singh, D. P., Uspal, W. E., Popescu, M. N., Wilson, L. G. & Fischer, P. Photogravitactic microswimmers. *Adv. Funct. Mater.* **28**, 1706660 (2018).
51. Zhang, J. et al. Photochemical micromotor of eccentric core in isotropic hollow shell exhibiting multimodal motion behavior. *Appl. Mater. Today* **26**, 101371 (2022).
52. Xiao, Z. et al. Synergistic speed enhancement of an electric-photochemical hybrid micromotor by tilt rectification. *ACS Nano* **14**, 8658–8667 (2020).
53. Oral, C. M., Ussia, M., Yavuz, D. K. & Pumera, M. Shape engineering of TiO<sub>2</sub> microrobots for “on-the-fly” optical brake. *Small* **18**, 2106271 (2021).
54. Lyu, X. et al. Active, yet little mobility: asymmetric decomposition of H<sub>2</sub>O<sub>2</sub> is not sufficient in propelling catalytic micromotors. *J. Am. Chem. Soc.* **143**, 12154–12164 (2021).
55. Gallego-Urrea, J. A., Tuoriniemi, J. & Hasselöv, M. Applications of particle-tracking analysis to the determination of size distributions and concentrations of nanoparticles in environmental, biological and food samples. *TrAC - Trends Anal. Chem.* **30**, 473–483 (2011).
56. Wilson, D. A., Nolte, R. J. M. & Van Hest, J. C. M. Autonomous movement of platinum-loaded stomatocytes. *Nat. Chem.* **4**, 268–274 (2012).
57. Novotný, F. & Pumera, M. Nanomotor tracking experiments at the edge of reproducibility. *Sci. Rep.* **9**, 13222 (2019).
58. Heckel, S. & Simmchen, J. Photocatalytic BiVO<sub>4</sub> microswimmers with bimodal swimming strategies. *Adv. Intell. Syst.* **1**, 1900093 (2019).
59. Ramirez Arenas, L., Ramseier Gentile, S., Zimmermann, S. & Stoll, S. Nanoplastics adsorption and removal efficiency by granular activated carbon used in drinking water treatment process. *Sci. Total Environ.* **791**, 148175 (2021).
60. Batool, A. & Valiyaveetil, S. Surface functionalized cellulose fibers – A renewable adsorbent for removal of plastic nanoparticles from water. *J. Hazard. Mater.* **413**, 125301 (2021).
61. Yen, P. L., Hsu, C. H., Huang, M. L. & Liao, V. H. C. Removal of nano-sized polystyrene plastic from aqueous solutions using untreated coffee grounds. *Chemosphere* **286**, 131863 (2022).
62. Urso, M. et al. Ultrasensitive electrochemical impedance detection of mycoplasma agalactiae DNA by low-cost and disposable Au-Decorated NiO nanowall electrodes. *ACS Appl. Mater. Interfaces* **12**, 50143–50151 (2020).
63. Vasilescu, A., Nunes, G., Hayat, A., Latif, U. & Marty, J. L. Electrochemical affinity biosensors based on disposable screen-printed electrodes for detection of food allergens. *Sensors* **16**, 1863 (2016).
64. Zhang, N., Halali, M. A. & de Lannoy, C. F. Detection of fouling on electrically conductive membranes by electrical impedance spectroscopy. *Sep. Purif. Technol.* **242**, 116823 (2020).
65. Urso, M. et al. Ni(OH)<sub>2</sub>@Ni core-shell nanochains as low-cost high-rate performance electrode for energy storage applications. *Sci. Rep.* **9**, 7736 (2019).
66. Yildiz, A., Lisesivdin, S. B., Kasap, M. & Mardare, D. Electrical properties of TiO<sub>2</sub> thin films. *J. Non Cryst. Solids* **354**, 4944–4947 (2008).
67. Luo, D., Liu, B., Gao, R., Su, L. & Su, Y. TiO<sub>2</sub>/CuInS<sub>2</sub>-sensitized structure for sensitive photoelectrochemical immunoassay of cortisol in saliva. *J. Solid State Electrochem.* **26**, 749–759 (2022).
68. Qi, X. Y. et al. Enhanced electrical conductivity in polystyrene nanocomposites at ultra-low graphene content. *ACS Appl. Mater. Interfaces* **3**, 3130–3133 (2011).

## Acknowledgements

M.P. was supported by Ministry of Education, Youth and Sports (Czech Republic) grant LL2002 under ERC CZ program. M.Ur. acknowledges the financial support by the European Union’s Horizon 2020 research and innovation program under the Marie Skłodowska-Curie grant agreement No. 101038066. This work was supported by the project Advanced Functional Nanorobots (reg. No. CZ.02.1.01/0.0/0.0/15\_003/0000444 financed by the EFRR). This work was supported by the ESF under the project CZ.02.2.69/0.0/0.0/18\_053/0016962. CzechNanoLab project LM2018110 funded by MEYS CR is gratefully acknowledged for the financial support of the measurements/sample fabrication at CEITEC Nano Research Infrastructure.

## Author contributions

M.Ur. designed, prepared, and characterized the microrobots, performed the analysis of the motion, the numerical simulation, and the electrochemical measurements, and wrote the manuscript. M.Ur. synthesized  $\gamma$ -Fe<sub>2</sub>O<sub>3</sub> nanoparticles and conducted nanoplastics’ capture experiments. M.Ur. and M. Us. carried out NTA with F.N.’s participation. M.Ur. and M.P. originated the idea. M.P. supervised the research. All authors have given approval to the final version of the manuscript.

**Competing interests**

The authors declare no competing interests.

**Additional information**

**Supplementary information** The online version contains supplementary material available at <https://doi.org/10.1038/s41467-022-31161-2>.

**Correspondence** and requests for materials should be addressed to Martin Pumera.

**Peer review information** *Nature Communications* thanks the anonymous reviewers for their contribution to the peer review of this work. Peer reviewer reports are available.

**Reprints and permission information** is available at <http://www.nature.com/reprints>

**Publisher's note** Springer Nature remains neutral with regard to jurisdictional claims in published maps and institutional affiliations.



**Open Access** This article is licensed under a Creative Commons Attribution 4.0 International License, which permits use, sharing, adaptation, distribution and reproduction in any medium or format, as long as you give appropriate credit to the original author(s) and the source, provide a link to the Creative Commons license, and indicate if changes were made. The images or other third party material in this article are included in the article's Creative Commons license, unless indicated otherwise in a credit line to the material. If material is not included in the article's Creative Commons license and your intended use is not permitted by statutory regulation or exceeds the permitted use, you will need to obtain permission directly from the copyright holder. To view a copy of this license, visit <http://creativecommons.org/licenses/by/4.0/>.

© The Author(s) 2022